



The July 20, 2017 M6.6 Kos Earthquake: Seismic and Geodetic Evidence for an Active North-Dipping Normal Fault at the Western End of the Gulf of Gökova (SE Aegean Sea)

ATHANASSIOS GANAS,¹  PANAGIOTIS ELIAS,² VASILIS KAPETANIDIS,³ SOTIRIOS VALKANIOTIS,⁴ PIERRE BRIOLE,⁵ IOANNIS KASSARAS,³ PANAGIOTIS ARGYRAKIS,¹ AGGELIKI BARBEROPOULOU,⁶ and ALEXANDRA MOSHOU¹

Abstract—On July 20, 2017 22:31 UTC, a strong $M_w = 6.6$ earthquake occurred at shallow depth between Kos Island (Greece) and Bodrum (Turkey). We derive a co-seismic fault model from joint inversion of geodetic data (GNSS and InSAR) assuming that the earthquake can be modelled by the slip of a rectangular fault buried in an elastic and homogeneous half-space. The GNSS observations constrain well most of the model parameters but do not permit to discriminate between south- and north-dipping planes. However, the interferograms, produced from C-band ESA Sentinel 1 data, give a clear preference to the north-dipping plane. We also map surface motion away from the satellite along the Turkish coast (from Bodrum towards the east) which reached about 17 cm onshore islet Karaada. The best-fit model is obtained with a 37° north-dipping, N283°E striking normal fault, in agreement with the published moment tensor solutions. The resolved slip vector is dominantly normal with a slight component of left-lateral motion (15°). The surface projection of the seismic fault outcrops in the Gökova ridge area, a well-developed bathymetric feature inside the western Gulf of Gökova. Our geodetic model fits the pattern of the shallow, north-dipping aftershocks obtained from rigorous relocation of all available recordings in the region (about 1120 events; relocated mainshock is at 36.955°N , 27.448°E ; depth at $9.2 \text{ km} \pm 0.5 \text{ km}$). The relocated aftershocks also indicate

clustering at both ends of the rupture and seismicity triggering mainly towards the east and the north, within 2 weeks following the mainshock. We also analysed regional GPS data (interseismic velocities) and obtained an extension rate of 3.2 mm/yr across the Gökova rift, along a direction N165°E.

Key words: Deformation, InSAR, GNSS, inversion, earthquake, Kos.

1. Introduction

On July 20, 2017 22:31 UTC (01:31 local time) a strong, shallow earthquake occurred offshore, east of the island of Kos, and south of the town of Bodrum, SE Aegean Sea (National Observatory of Athens—NOA magnitude $M_w = 6.6$, EMSC & USGS $M_w = 6.6$; Ganas et al. 2017a, 2018; Saltogianni et al. 2017; Tiryakioğlu et al. 2018; Ocakoğlu et al. 2018; Kiratzi and Koskosidi 2018; Karasözen et al. 2018; Fig. 1). This is the largest event in the area since the destructive Kos earthquake of April 23, 1933 (Kouskouna et al. 2017) which was of surface magnitude $M_s = 6.4$ (Ambraseys, 2001) or moment magnitude $M_w = 6.5$ (Makropoulos et al. 2012). The 2017 earthquake registered VI–VII instrumental intensities <https://shake.gein.noa.gr/sm/noa2017odde/intensity.html>; last accessed 2 Jun 2018), and caused severe damage to the building stock of Kos including partial collapses that killed two people and seriously injured several others. Among the secondary effects it is worthy to mention (a) soil spreading that caused damage to the port of the town of Kos (Papathanassiou et al. 2019) and (b) a local tsunami that flooded part of the towns of Bodrum and Kos (Fig. 1; Yalçiner et al. 2017) and hit the nearby coastlines. No

Electronic supplementary material The online version of this article (<https://doi.org/10.1007/s00024-019-02154-y>) contains supplementary material, which is available to authorized users.

¹ National Observatory of Athens, Institute of Geodynamics, Lofos Nymfon, Thission, 11810 Athens, Greece. E-mail: aganas@noa.gr; pargyrak@noa.gr; amoshou@noa.gr

² National Observatory of Athens, Institute of Astronomy, Astrophysics, Space Applications and Remote Sensing, Lofos Nymfon, Thission, 11810 Athens, Greece. E-mail: pelias@noa.gr

³ National and Kapodistrian University of Athens, Faculty of Geology and Geoenvironment, University Campus- Zografou, Athens 157 84, Greece. E-mail: vkapetan@geol.uoa.gr; kassaras@geol.uoa.gr

⁴ Koronidos Str, 42131 Trikala, Greece. E-mail: valkaniotis@yahoo.com

⁵ Ecole Normale Supérieure, PSL research University, Laboratoire de Géologie-UMR CNRS 8538, Paris, France. E-mail: briole@ens.fr

⁶ AIR Worldwide, Research Department, 131 Dartmouth St, Boston, MA 02116, USA. E-mail: aggeliki.barberopoulou@gmail.com

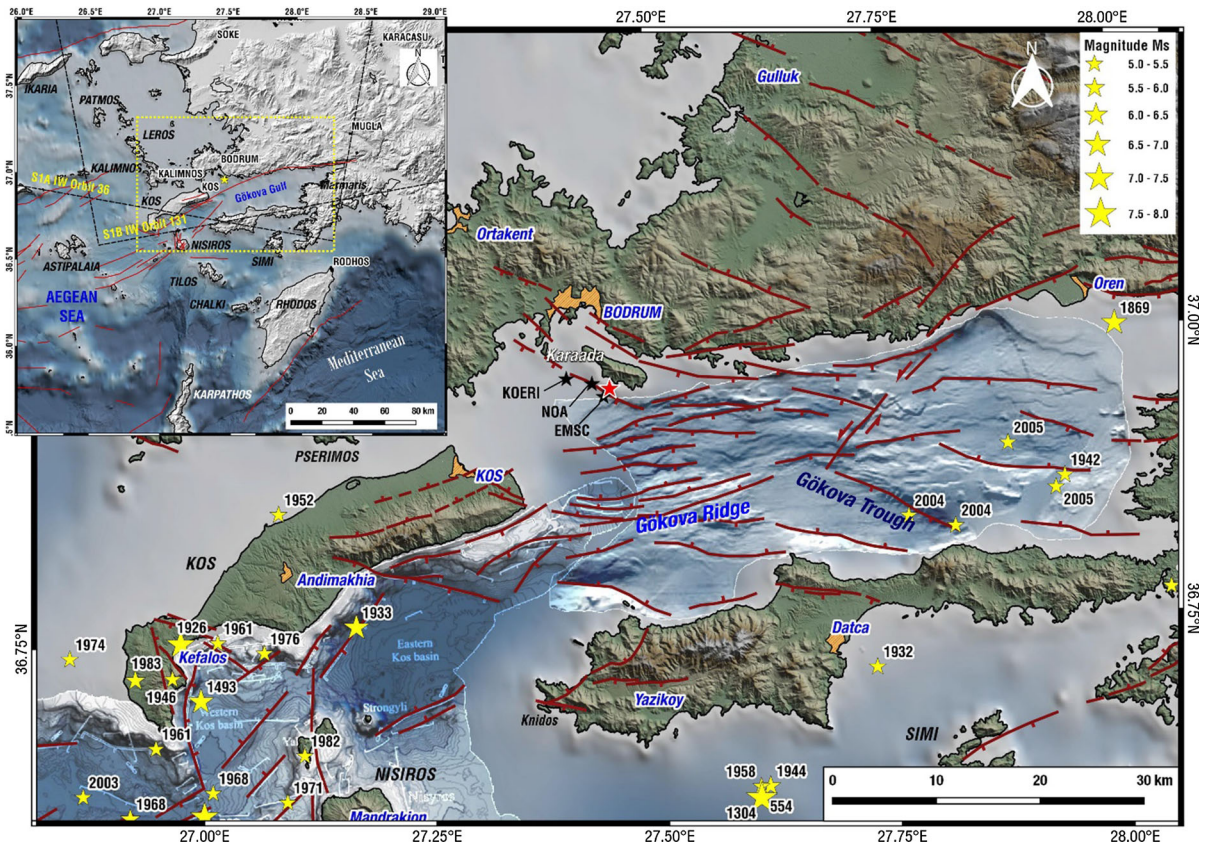


Figure 1

Location map and relief model of the region affected by the Kos earthquake (20/7/2017 22:31 UTC; $M_w = 6.6$) in the SE Aegean Sea. Red star indicates the relocated epicentre (this study) black stars denote manual epicentre determinations of the mainshock by NOA, KOERI and EMSC. Red lines are active faults from various sources including Ganas et al. (2013a), Nomikou et al. (2013), İşcan et al. (2013) and Tur et al. (2015). Yellow stars show epicentres of historical and instrumental earthquakes with $M > 5.0$ (from Papazachos and Papazachou 1997; star size is proportional to earthquake magnitude). Land elevation was obtained from ALOS GSDM and bathymetry was combined from data of EMOINET, Nomikou (2004) and İşcan et al. (2013). Inset box at upper left shows location of the study area within the South Aegean Sea and Sentinel-1 satellite frames (black boxes; only part of the 250 km frame is shown)

extensive landsliding was reported in either Greece or Turkey and our investigation of Sentinel 2 imagery (July 22 and 24 acquisitions) showed no landslide scars inland. The strongest aftershock occurred on 8 August 2017 07:42:21 UTC ($M_{w(NO A)} = 5.2$).

The 2017 epicentre was determined near the uninhabited islet of Karaada, offshore Bodrum, SW Turkey (Fig. 1) by the following institutes operating the main seismic networks in the region, i.e.: NOA at $36.96^\circ\text{N } 27.43^\circ\text{E}$, EMSC at $36.96^\circ\text{N } 27.45^\circ\text{E}$, KOERI at 36.96°N and 27.41°E . The focal mechanisms of the mainshock (Table 1; Fig. 2) indicate normal faulting with nearly E–W strike, moderate dip angles. A small, left-lateral component of the slip

vector is reported by the majority of the solutions. The dip-direction of the fault plane was determined as north-dipping by Ganas et al. (2017a, 2018), Konca et al. (2018) and Karasözen et al. (2018) while Saltogianni et al. (2017), Tiryakioğlu et al. (2018), Ocakoğlu et al. (2018) and Kiratzi and Koskosidi (2018) proposed a south-dipping plane.

The Kos earthquake occurred in a region of predominantly extensional tectonics as evidenced by the formation of Quaternary marine grabens, namely the NE–SW Kos graben (Tibaldi et al. 2008; Nomikou and Papanikolaou 2011, 2013) and the east–west trending Gökova graben (Ulug et al. 2005; Tur et al. 2015; Ocakoğlu et al. 2018; Fig. 1). The Gökova

Table 1

Moment tensor solutions for the mainshock reported at the EMSC website by various seismological institutions

Institute	M _w	M ₀ (*E + 18 Nm)	Depth (km)	Nodal plane 1			Nodal plane 2		
				Strike (°)	Dip (°)	Rake (°)	Strike (°)	Dip (°)	Rake (°)
GCMT	6.6	9.7	12	275	36	- 85	89	54	- 94
CPPT	6.7	14.2	10	290	26	- 58	76	68	- 104
IPGP	6.6	9.7	9	284	32	- 71	82	60	- 102
GFZ	6.6	9.7	11	270	56	- 94	98	35	- 82
USGS	6.6	11.0	11.5	285	39	- 73	84	53	- 103
KOERI	6.6	11.3	6	286	53	- 72	78	40	- 112
INGV	6.7	13	11.3	296	49	- 55	68	52	- 124
NOA	6.6	8.9	6	265	43	- 102	102	48	- 79
AUTH	6.5	8.9	7	275	41	- 88	93	49	- 91
NKUA	6.6	8.9	11	267	38	- 110	112	55	- 75
Average		10.6	9.5	279	41	- 81	89	52	- 96
r.m.s scatter		1.8	2.2	10	9	17	13	9	14

The full name of each institute is given in Supplementary Table S3

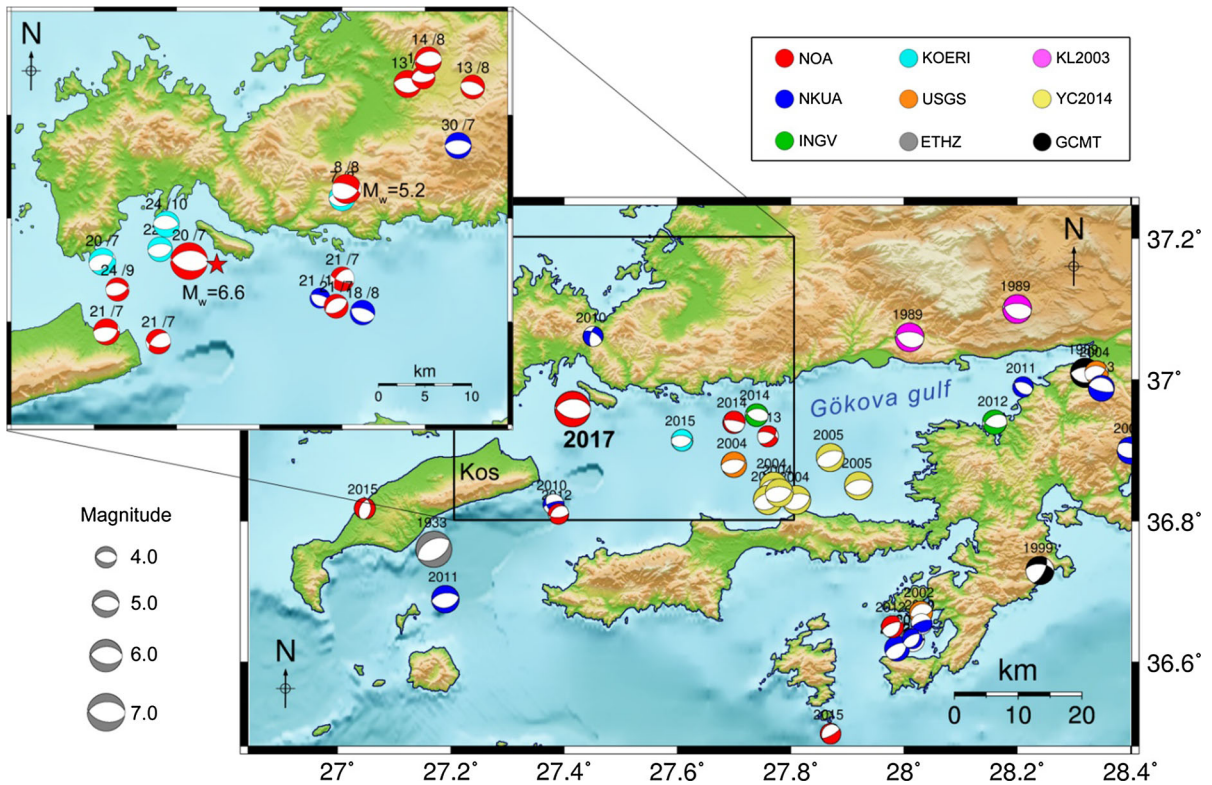


Figure 2

Map of the Gökova Rift showing focal mechanisms (beach balls) of strong earthquakes, colour coded according to the reporting institution (info is given on upper right; period 1976–2017). Only events with focal depth < 60 km are shown. The data indicate predominantly normal-slip character of seismic faulting. Upper left box shows the relocated epicentre (red star) and the focal mechanisms of the strongest aftershocks of the 2017 seismic sequence (date is given above beachball). KL2003: Kiratzi and Louvari (2003); YC2014: Yolsal-Çevikbilen et al. (2014)

Gulf (*Kerameikos* in Greek) is an E–W extensional basin that is believed to have developed during two episodes of rift formation (Görür et al. 1995; Tur et al. 2015). Its primal form originated during Upper Miocene–Pliocene, due to the regional N–S extension and the development of the normal Datça fault to the south (Kurt et al. 1999; Uluğ et al. 2005; İşcan et al. 2013). In the second phase, during Pliocene–Pleistocene a new series of E–W normal faults developed a more complex pattern of basins and ridges and led to the formation of the main Gökova rift (Tur et al. 2015). These faults define the present-day shoreline of Gökova Gulf. To the north of Gökova Gulf, there is a series of inland basins controlled by NW–SE to WNW–ESE normal/normal-oblique faults. These basins are also synchronous to the main Gökova rift opening and growth during Pliocene–Pleistocene, and host Miocene–Pliocene formations (Gürer and Yilmaz 2002; Gürer et al. 2013).

Seabed morphology and offshore structure of the central and eastern part of the Gökova Gulf has been surveyed by seismic reflection profiles and multibeam bathymetry (Kurt et al. 1999; Uluğ et al. 2005; İşcan et al. 2013, Tur et al. 2015). The south-west region that connects the Gökova Gulf with the Kos–Nisyros graben has been also surveyed (Nomikou 2004; Ocakoğlu et al. 2018). A gap of offshore data exists for the north-western part between Bodrum and Kos. The tectonic interpretation of both seismic profiles and bathymetric features varies in literature. Most authors suggest that the western-central part of the Gökova Gulf is dominated by multiple WNW–ESE extensional faults dipping mainly to the south. Moreover, recent offshore seismic data provide evidence for strike-slip motions on young structures (İşcan et al. 2013; Ocakoğlu et al. 2018).

In the greater Kos–Bodrum region the present-day crustal deformation measured by GNSS is extensional with a N–S ($\pm 10^\circ$) orientation (Kreemer and Chamot-Rooke 2004; Floyd et al. 2010; data from extensional strain axes patterns). A 4 mm/year extension rate across the Gulf of Gökova has been suggested by Vernant et al. (2014). A component of strike-slip tectonics is also expected in this region because of the interaction of the Aegean microplate with the down-going Nubia plate (Ganas and Parsons 2009, their Fig. 6).

The extensional tectonics is also demonstrated by various seismological data, mainly earthquake focal mechanisms (i.e. Kiratzi and Louvari 2003; Irmak 2013; Yolsal-Çevikbilen et al. 2014; Friederich et al. 2013). Focal mechanisms of extensional character are also reported in databases of various seismological institutes on the internet; see Fig. 2 and Supplementary Table S3 for full list). The majority of the focal mechanisms of strong earthquakes in the Gökova rift (Fig. 2; period 1976–2017) indicate that the minimum compressive stress direction is horizontal and oriented approximately N–S, in agreement with geodetic data. Most focal mechanisms originate from the NOA database (especially for the 2017 aftershock sequence) and the National Kapodistrian University of Athens (NKUA) database. In both cases the published solution is the result of manual processing with regional waveform modelling (e.g. Papadimitriou et al. 2012); for NOA a well-established procedure that employs the ISOLA software (Sokos and Zahradnik 2008) is being used. A few focal mechanisms from GCMT (<http://www.globalcmt.org/>) are also derived using well-established waveform inversion procedures.

In this work we use geodetic data (Sect. 2; co-seismic InSAR observations and GNSS co-seismic offsets) and relocation of seismic data (Sect. 4) to infer the dip-direction of the 2017 seismic fault and refine parameters such as its location, geometry, and amount of slip. Our displacement data were added to those of Tiryakioğlu et al. (2018), allowing us to compile a comprehensive set of GNSS co-seismic offsets (Table 2). Those vectors are used to infer the fault parameters by inversion. Then, we process the InSAR Sentinel 1A raw data to obtain co-seismic interferograms for both orbits (ascending and descending). We combine GNSS and InSAR displacements to improve the quality of our inversion (Sect. 3). We then analyse earthquake recordings in order to precisely locate the mainshock and the aftershock sequence. As our study is focused on data inversion towards identifying the fault plane and not towards the physics of the earthquake source, we do not perform further moment tensor inversion of the mainshock or of the large aftershocks. By combining the data sets from space geodesy and seismology we find that the earthquake occurred at a 37-degree,

Table 2

Co-seismic GNSS displacements and uncertainties

Code	Array	Long	Lat	dE (mm)	dN (mm)	dU (mm)	Source
086A	HEPOS	27.1477	36.7863	-9 ± 3	-10 ± 3	16 ± 9	
087A	HEPOS	28.0049	36.3645	3 ± 3	-5 ± 3	-8 ± 9	
ASTY	Metrica	26.3533	36.5451	-2 ± 4	-1 ± 4	2 ± 12	
AYD1	CORS-TR	27.8378	37.8407	2 ± 4	4 ± 4	-7 ± 15	a
BODR	Campaign	27.401	37.019	-38 ± 9	160 ± 9	119 ± 22	a
CAMK	Campaign	27.8359	37.1965	2 ± 5	28 ± 6	28 ± 21	a
CESM	CORS-TR	26.3726	38.3038	0 ± 3	1 ± 3	-6 ± 11	a
DATC	CORS TR	27.6918	36.7086	10 ± 5	-32 ± 5	8 ± 15	
DIDI	CORS TR	27.2687	37.3721	-5 ± 5	19 ± 5	2 ± 15	
FETH	CORS-TR	29.1238	36.6262	-1 ± 3	2 ± 3	-5 ± 13	a
IKAR	Tree	26.2733	37.6054	-5 ± 6	-1 ± 6		
IZMI	CORS-TR	27.0818	38.3948	1 ± 3	1 ± 3	-2 ± 10	a
KALU	Tree	26.9617	36.9624	-7 ± 6	-1 ± 6		
KALM	Metrica	26.9762	36.9558	-3 ± 4	0 ± 4	11 ± 12	
KNID		27.3939	36.6822	-20 ± 4	-50 ± 4	-2 ± 16	a
KRP1	Metrica	27.1203	35.4805	0 ± 4	-4 ± 4	5 ± 12	
KY CZ	Campaign	28.6864	36.9788	12 ± 9	6 ± 9	10 ± 30	a
MARM	Campaign	27.9628	36.7726	6 ± 3	-2 ± 3	6 ± 10	a
MUG1	CORS TR	28.3557	37.2143	0 ± 5	-4 ± 5	6 ± 15	
MUMC	Bodrum CORS	27.619	37.1387	23 ± 2	69 ± 3	4 ± 10	a
ORTA	Bodrum CORS	27.3486	37.0508	-39 ± 2	100 ± 3	15 ± 9	a
ROD0	Tree	28.1953	36.4023	-1 ± 6	-11 ± 6		
ROD2		27.9231	36.0209	2 ± 2	-6 ± 2	6 ± 10	a
SAMU	Tree	26.9734	37.7575	-9 ± 6	1 ± 6		
SAMM	Metrica	26.7054	37.7927	-4 ± 4	1 ± 4	6 ± 12	
TGRT	Bodrum CORS	27.2568	37.0071	-9 ± 3	25 ± 3	1 ± 11	a
TRKB	Bodrum CORS	27.3226	37.1139	-25 ± 2	65 ± 2	3 ± 9	a
YALI	Bodrum CORS	27.5353	36.995	7 ± 3	153 ± 3	7 ± 11	a

Data from various networks, NOA, HEPOS-GR, METRICA-GR, TREE Co-GR, GEOTEKNIK-TR, CORS-TR (see Fig. 3 for location). Source (a) is from Tiryakioğlu et al. (2018), all others determined in this study

north-dipping fault. This is an important result for understanding the tectonics and Quaternary evolution of the Gulf of Gökova rift.

2. Geodetic Data and Methods

2.1. GNSS Data Processing

We processed GNSS data (30-s sampling interval) from the following permanent networks: NOA (Ganas et al. 2008, 2011), TREE (commercial provider in Greece; <http://uranus.gr/>), METRICA (commercial provider in Greece; <http://www.metricanet.gr/>), HEPOS (<http://www.hepos.gr/>; Gianiniou, 2011), and GCM from Turkey (DATC, DIDI, MUG1). The location of the GNSS stations is shown in Fig. 3. The data were processed with the GIPSY/

OASIS II software (ver. 6.4) developed by Jet Propulsion Laboratory (JPL; <http://gipsy-oasis.jpl.nasa.gov/>; Bertiger et al. 2010). This software is using a Precise Point Positioning strategy (Zumberge et al. 1997). We used the orbit and clock files of highest precision (*flinnR files*). We applied absolute antenna calibration, random walk troposphere estimation and we used the FES2004 tidal coefficients for the ocean loading modelling. Additional GNSS data were provided by Tiryakioğlu et al. (2018) acquired at GEOTEKNIK and other CORS-Turkey permanent stations and campaign stations. The co-seismic displacements are listed in Table 2 and are plotted in Fig. 3. At the stations processed by both Tiryakioğlu et al. (2018) and us, the consistency between the solutions is better than 4 mm on average. For our modeling purposes (see next section) this

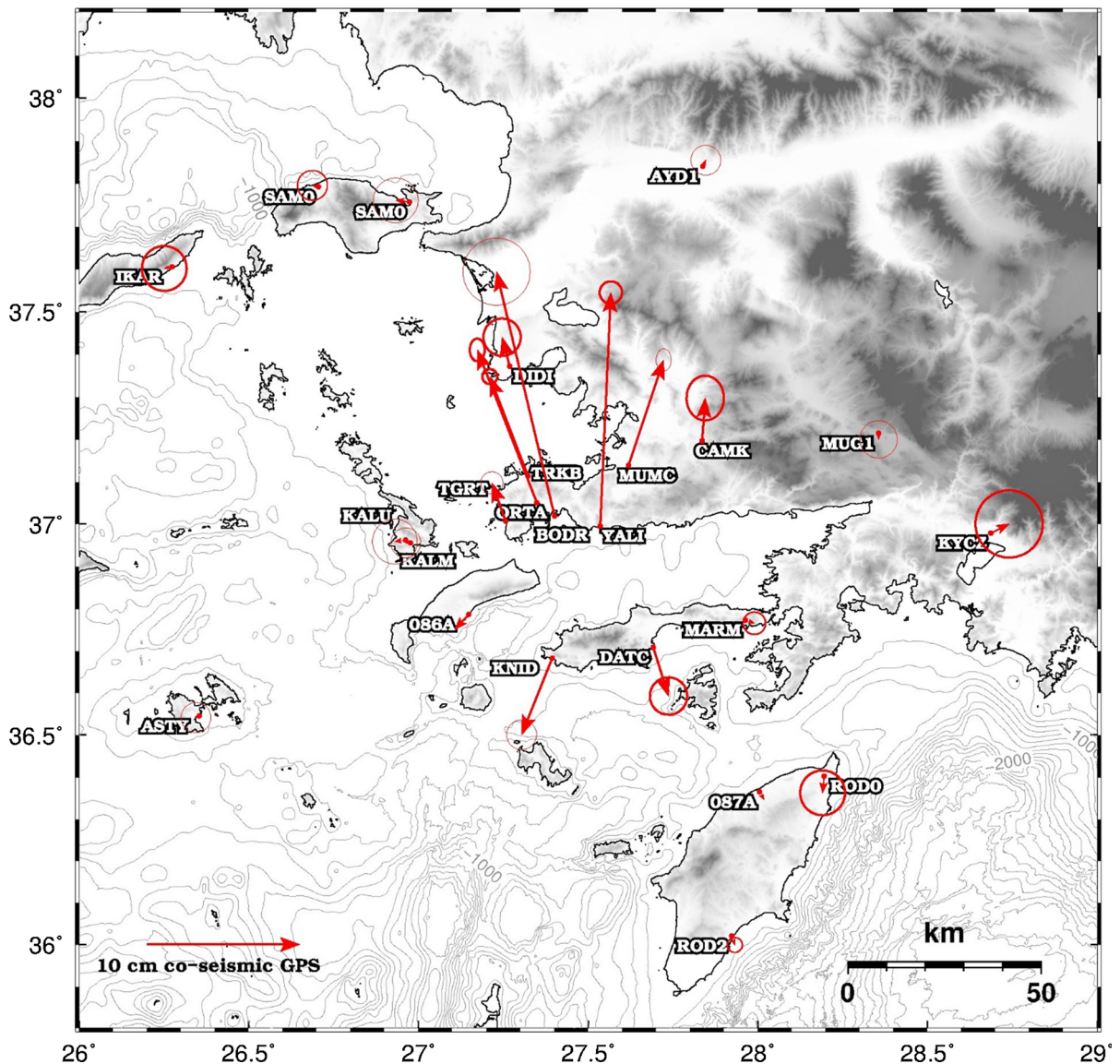


Figure 3

Horizontal co-seismic offsets (red vectors) with 95% confidence ellipses due to the 2017 Kos earthquake. The station name is reported at the base of each vector. The displacement data are shown in Table 2

difference of 4 mm is not significant and has no impact in our conclusions.

2.2. INSAR Data Processing

2.2.1 Calculation of Interferograms

We used Sentinel 1A/1B Terrain Observation with Progressive Scans (TOPS) acquisitions from ESA

(Sentinel 1A/1B satellite data; C-band). One fringe corresponds to half wavelength, i.e. 28 mm. The SAR data were acquired every 6 days between June 30, 2017 and October 10, 2017 along the ascending track 131 and the descending track 36. The view azimuth is almost opposite for ascending and descending tracks (Fig. 4 top, bottom).

Using the ESA SNAP software and the SRTM digital elevation model (DEM) at 90 m resolution, we

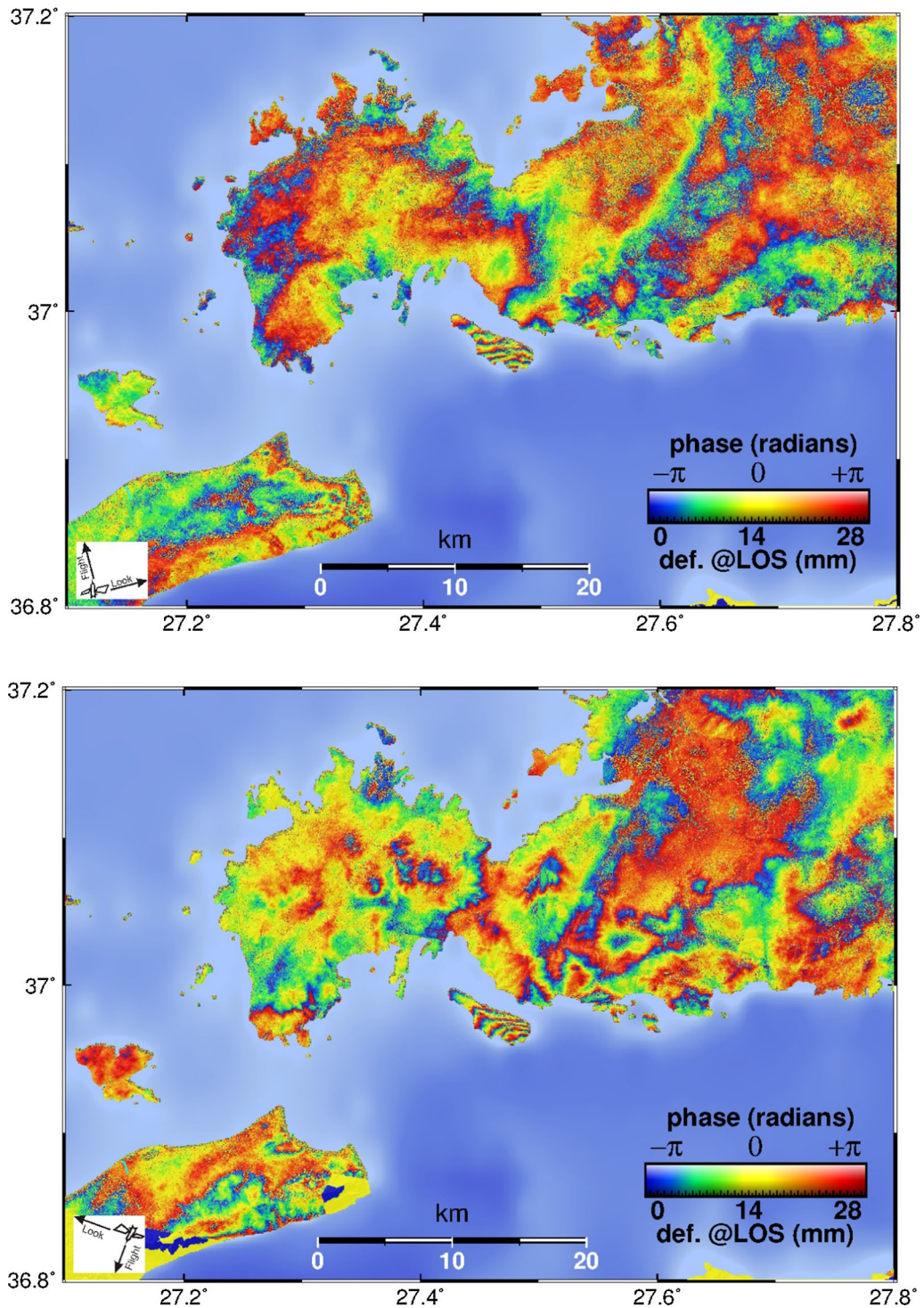


Figure 4

InSAR processing results: (top) Sentinel 1A wrapped interferogram ascending orbit Track 131 acquisition dates: 12/7/2017–24/7/2017
(bottom) descending orbit Track 36 acquisition dates: 18/7/2017–24/7/2017

produced approximately 20 pre-seismic, 60 co-seismic, and 140 post-seismic interferograms. Each interferogram is a map (wrapped at the wavelength of 28 mm) of the ground motion in the line-of-sight (LOS) of the satellite. Multi-looking was applied using a factor of 2:6 (azimuth and range) to further reduce the noise level and obtain an approximately square pixel. Most of the interferograms have good coherence. The low coherent areas correlate with the vegetated areas. In several cases there are significant tropospheric effects in the mountainous areas. The geodetic accuracy of the interferograms is limited more by the troposphere than by the coherence.

The interferograms show a clear signal with eight (8) fringes in the ascending track and seven (7) fringes in the descending track, mostly localised in the Karaada islet, offshore Bodrum (Figs. 1, 4). The islet is located near the epicentre. The peak LOS change, approximately 0.17 m away from the satellite in both descending and ascending views, is observed at the southeast coast of the islet. The co-seismic deformation has a similar pattern for all co-seismic interferograms having the second image acquired before early August (approx. 2 weeks following the mainshock). Conversely, in the interferograms spanning after early August (starting on August 5, 2018), a clear and localized fringe (~ 30 mm) is visible at the north coast of the gulf near YALI (Fig. 3) east of Bodrum. As the aftershocks (up to $M_L = 4.8$; NOA magnitude) that occurred in the first two weeks, mostly offshore, produced no signature in the interferograms, we conclude that the $M_{6.6}$ Kos earthquake was not followed by detectable short-term post-seismic motion within the uncertainty range of ± 5 mm.

2.2.2 Picking of the Co-Seismic Fringes

Four ascending (2017 June 30–July 30, 2017 July 12–July 24 seen in Fig. 4 top, 2017 July 12–July 30, and July 18–July 24) and four descending (2017 July 6–July 24, July 6–July 30, July 18–July 24 seen in Fig. 4 bottom, and July 18–July 30) co-seismic interferograms were analyzed more carefully because of their short time span that maximizes signal phase coherence and minimizes possible post-seismic signal. We found that this number of four (in each track)

was a good compromise so as to verify that (a) the differential tropospheric effect, from one to another interferogram, was not affecting the picking, and (b) to pick a signal mostly co-seismic.

We picked 67 points on the ascending interferograms on eight different fringes corresponding to displacements along the line of sight ranging from +28 mm to -168 mm, and 86 points on the descending interferograms on seven different fringes corresponding to displacements along the line of sight ranging from 0 mm to -168 mm (see Supplementary Fig. S2 and Fig. S3 for location of picked points). The zero value of the pickings was based on the synthetic interferograms predicted from the inversion of the GNSS data only (see Sect. 3.1). The use of the zero-value prediction from GNSS is efficient to assess the continuity of fringes between Karaada islet and the mainland. Indeed, even if this prediction is slightly biased in absolute terms, its spatial derivative is in general very robust in any local area (along the north coast or onshore Karaada). In order to better constrain the location of the western side of the fault we added, for both ascending and descending views, eight arbitrary pickings along the west coast of Kos (see Supplementary Fig. S2). We set a zero value to those points as no fringe is clearly visible in Kos.

3. Seismic Fault Inversion from Geodetic Data

We assume that the earthquake can be modelled with a homogeneous slip on a rectangular fault buried in an elastic half-space. The fault is described by nine parameters (Okada 1992; Briole et al. 1986; Briole 2017): the three coordinates of the centre of the upper edge of the fault, the length and width of the fault, the azimuth (strike), dip and rake angles, and the slip. A priori values of the three angles are provided by seismology through the centroid moment tensors (CMT) along with values of the seismic moment. Table 1 gives a list of determinations of CMT and their average and standard deviations that we used in our model without inverting two of them; the azimuth and the dip angles. We invert for the rake and the other 6 parameters (coordinates and size of the fault, and amount of slip). For modeling purposes and

comparison with seismological data, we assume that the rigidity of the crust is 3×10^{10} N m.

In our inversion algorithm the equations that link the fault parameters to the displacements are not linear but they can be approximated as linear equations around any particular set of parameters, especially when the fault does not reach the surface as it is in our case. Our inversion algorithm is based on local linear inversion performed in an iterative manner (5 iterations in this case), with the partial derivatives recalculated at each iteration step.

3.1. Inversion of the GNSS Data

InSAR and GNSS data have different status and importance for constraining fault parameters. In this first step we use GNSS only. The GNSS coverage at the broad scale is remarkably good for this earthquake since GNSS co-seismic vectors are available in all azimuths, at different distances, with large amplitudes at several stations (Fig. 3). Therefore, they constrain very efficiently all fault parameters. In all inversions performed, from any set of a priori parameters, the inversion is stable, yielding the same solution. However, the GNSS observations did not allow us to discriminate between south- and north-dipping candidate planes, leading to two antithetic solutions with almost equal goodness of fit. Nevertheless, the fit is slightly better for the north-dipping case (see the root mean square - r.m.s. values in Table 3). The vertical component at station YALI, about 7 km NE of the epicentre (Fig. 3) indicates a much better fit for a north-dipping (Supplementary Table S1), than a south-dipping (Supplementary Table S2) plane. But as YALI is the only GNSS point where the vertical motion can discriminate

between the two planes, this constraint is not very robust.

The predicted geodetic moment and the rake fit well with the seismological ones. The north-dip case, predicts a component of left-lateral strike-slip on the fault plane. The r.m.s. scatter for the horizontal and vertical components of the GNSS vectors are small and consistent with the a priori values used for the inversion (4 and 10 mm; or the “a priori uncertainties” used as input in the inverse algorithm). These values are consistent with both the formal uncertainties from our own GNSS processing and from the scatters between our vectors and the Tiryakioğlu et al. (2018), vectors. The predicted slip amount is large but not unusual, given the $M_w = 6.6$ magnitude and the inferred small size of the fault, especially for the north-dipping case.

In the inversion there is a trade-off between the amount of slip on the fault and the fault width and we found that solutions with fault width larger by up to 30% (i.e. 8.7 km) and corresponding slip lower by up to 30% (i.e. 2.24 m) lead to residuals not much larger than the optimal one. The GNSS data show clearly that the rupture did not reach the surface: its modeled top edge is between 2 and 3 km depth. The parameters of the best fitting models deduced from GNSS only for both south- and north- dipping cases are listed in Table 3.

3.2. Rejection of the South Dipping Model from Joint Inversion of GNSS and InSAR

In the previous section we have seen that GNSS constrains well all the parameters of the fault and favors, but very slightly, the north-dipping case. The robust discrimination between south- and north-

Table 3

Best fitting fault models when using only GNSS data

Dip-direction	Long (°)	Lat (°)	U (km)	L (km)	W (km)	Slip (m)	Az. (°)	Dip (°)	Rake (°)	Moment (10^{18} Nm)	Centroid depth (km)	r.m.s. hor. (mm)	r.m.s. vert. (mm)
North	27.475	36.907	3	16.6	6.7	2.91	279	41	- 80	9.7	5.2	3.2	12.3
South	27.486	36.957	2.9	19.2	8.6	2.07	89	52	- 93	10.3	6.3	3.3	13.9

The LONG-LAT coordinates are for the middle of fault top edge

Parameter U indicates the depth to the middle of the top edge

dipping cases comes from SAR interferometry. Indeed, the predicted fringes pattern in the Karaada islet is very different in the two cases. In the north-dipping hypothesis, because the fault is located deep below the island, the modeled distance between fringes is relatively steady from the south to the north of the islet and never dense. In the south-dipping hypothesis, because the fault tip arrives close to the island, the modeled fringe pattern is much denser and with an inter-fringe distance that varies significantly perpendicularly to the fringes.

For the joint inversion, we used a modified version of our code (Briole 2017) with a priori uncertainties set at 4 mm for the horizontal GNSS components and 10 mm for the vertical GNSS component and InSAR. We checked that the solutions remained almost identical when modifying those values in the range 3–5 mm and 8–20 mm, respectively. The ratio between the number of picked points (153 + 8 in Kos) and the number of GNSS points (28), weighted by the a priori uncertainties, gives approximately the same weight to InSAR and horizontal GNSS in the inversions. The best fitting models determined by the joint GNSS and InSAR inversions are summarized in Table 4. Supplementary Tables S1 and S2 contain the observed and modelled GNSS displacements in both north-dipping and south-dipping cases.

The best south-dipping model predicts a fringe pattern not consistent with several observations (Fig. 3; Fig. 4, bottom): (a) the fringe pattern is predicted too dense in the Karaada islet, (b) for the ascending view, the model predicts fringes along the west coast of Kos that are not observed in reality, (c) the azimuth and bending of the fringes are less

consistent with observations than those predicted in the north-dipping case. Finally, the fit of the GNSS vectors is clearly worse, especially in the north–south component where the misfits are three times larger than in the north-dipping case. Moreover, in the south-dipping case, the inversion was not stable for the fault width, which decreased to the unrealistic value of 3.5 km, in which case we were obliged to apply an arbitrary value. We tested the range 6–9 km and used 7 km to make the inversion stable for all other parameters. The main differences of joint GNSS-InSAR inversion with respect to the GNSS-only are an increase of the fault length at 21.2 km and a deepening of the fault tip at 4.6 km (see Table 4 and Fig. 6a for a map view). This deepening in the south-dip model is needed to reduce the density of modeled fringes in the Karaada islet.

On the other hand, in the case of the north-dipping fault, we found all inversions stable for all parameters and best fit to both InSAR and GNSS. The north-dipping plane is strongly supported by the InSAR data (see Fig. 5 for a goodness of fit comparison between picked and modeled values; representation introduced by Briole et al. 2015) and above all by the consistency between GNSS and InSAR in the inversion. The main changes when adding InSAR to GNSS are a decrease of the fault length and an increase of its width. The top edge of the fault is now at 2.5 km depth and its bottom at 9.9 km depth (Table 4; Fig. 6b). For comparison, we present both models in map view (Fig. 6a) and along a N–S cross-section (Fig. 6c). We note that we could not find another set of published parameters (last literature search on 11 June 2018) for the south-dip case (as those we provide in Table 4).

Table 4

Best fitting models from the joint inversion GNSS & InSAR (28 GNSS points, 67 ascending pickings, 86 descending pickings)

Dip	Long (°)	Lat (°)	U (km)	L (km)	W (km)	Slip (m)	Rake (°)	Moment (10 ¹⁸ Nm)	Centroid depth (km)	r.m.s. hor. (mm)	r.m.s. vert. (mm)	r.m.s. ascend. (mm)	r.m.s. desc (mm)
North	27.481	36.879	2.4	11.8	10.3	2.94	− 79	10.7	5.8	4.6	15.0	5.0	11.0
South	27.480	36.946	4.6	21.2	7.0	2.12	− 105	9.4	7.4	12.7	12.0	8.8	12.1

Azimuth and dip angles are the same as in Table 3. The LONG-LAT coordinates are for the middle of fault top edge. Parameter U indicates the depth to the middle of the top edge

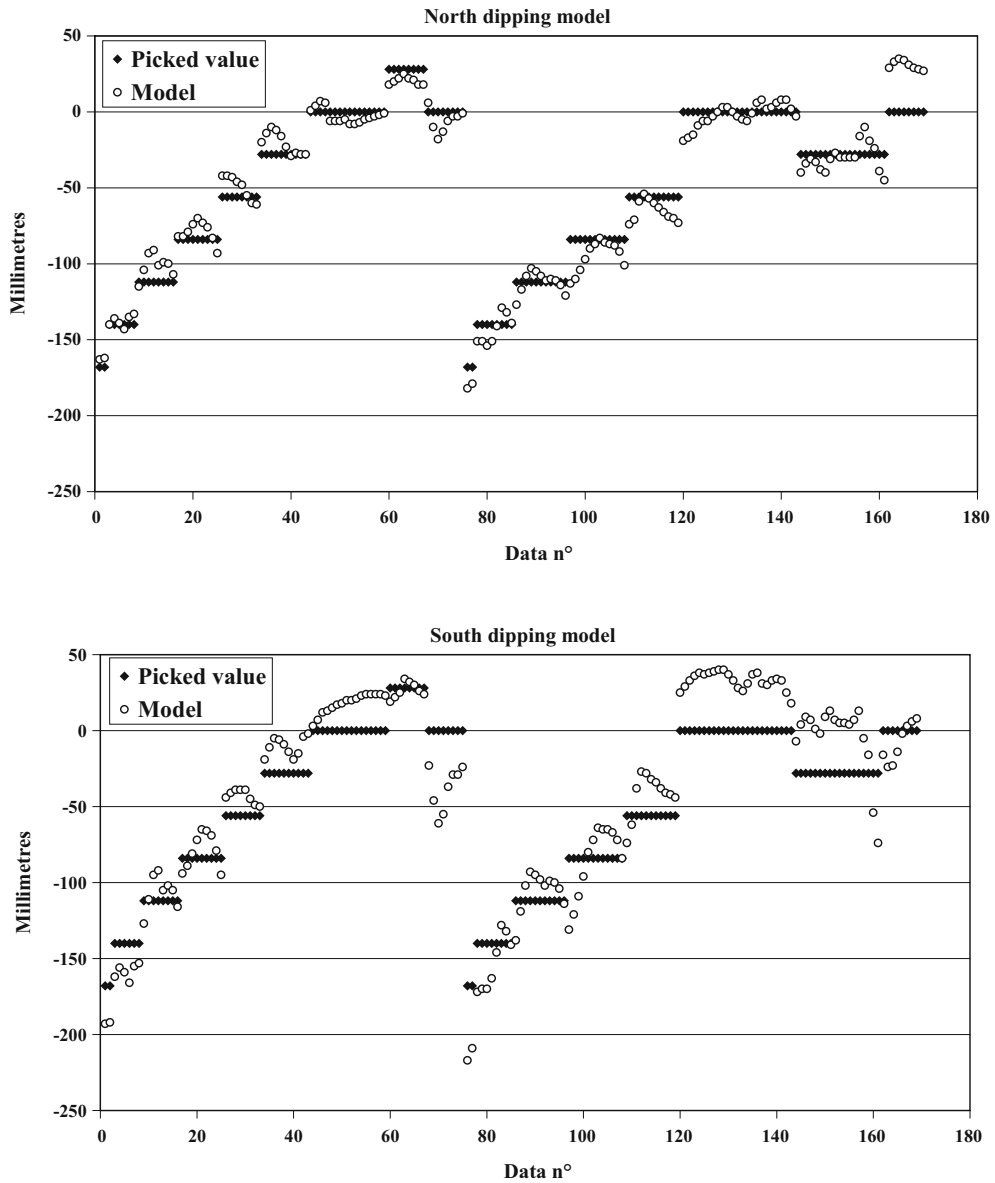


Figure 5

Diagrams showing goodness of fit between picked (black dots) and modelled displacements (open circles). Top: fit of the InSAR data in the north-dipping model (ascending data are on the left side and descending on the right side), bottom: fit of the InSAR data in the south-dipping model (ascending data are on the left side and descending on the right side). Descending/Ascending track picked points are visible in Supplementary Fig. S2 and Fig. S3 respectively

3.3. Best Fitting North Dipping Model from Joint Inversion of GNSS & InSAR

In the previous section we have rejected the south-dipping case as it is not supported by the InSAR data. Here, in a further refined step, performed for the north-dipping case only, we allow all nine

parameters to vary in the inversion (instead of only seven before). The inversion is stable and the azimuth and dip angles rotate slightly by 3° each, the rake changes slightly to balance the change of the azimuth (indeed, azimuth and rake are strongly coupled). The parameters of this final model, listed in Table 5, are

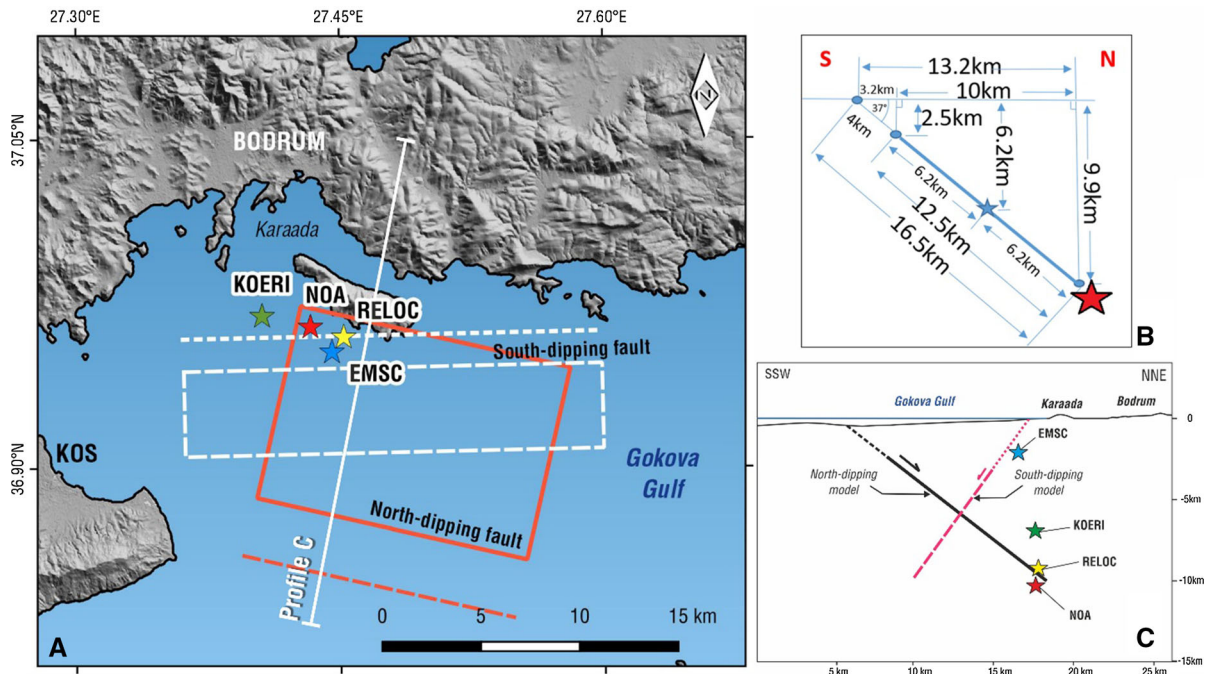


Figure 6

Fault model plots: **a** map showing surface projections of south-dipping fault (white rectangle) and north-dipping fault (red rectangle); dotted lines mark the ground surface intersection of the fault planes. **b** Schematic section across the modelled fault (red rectangle), red star indicates relocated mainshock hypocentre on the lower (northern) fault edge **c** NNE-SSW profile (scale 1:1) showing both fault planes and projected hypocentres of the mainshock. The south-dipping plane parameters are those of Table 4 (this study). The north-dipping plane better satisfies the seismological data as the south-dipping fault (red dashed line) is incompatible with the projection of hypocentres (situated at its footwall, about 7–8 km away from its down-dip trace)

Table 5

Best fitting fault model, and its uncertainties, from the joint inversion of GNSS & InSAR

Long (°)	Lat (°)	Top (km)	Length (km)	Width (km)	Slip (m)	Azimuth (°)	Dip (°)	Rake (°)	Moment (10^{18} Nm)	Centroid depth (km)
27.479	36.872	2.5 ± 0.2	14.0 ± 1.0	12.5 ± 1.0	2.03 ± 0.3	283 ± 3	37 ± 3	-75 ± 3	11.0 ± 0.5	6.2 ± 0.3

Geographic coordinates (LON, LAT; in decimal degrees) refer to the middle of the top edge of the fault

not very different from the ones of Table 4. This best fitting model is a blind fault, buried at 2.5 km depth with bottom at 9.9 km depth, and a relatively large slip of 2.07 m. The vertical r.m.s., 5.1 mm, is the one calculated without the GNSS station BODR that is an outlier, otherwise it becomes 13.7 mm. The other r.m.s. are 4.2 mm for the horizontal GNSS and 7.2 mm for the InSAR observations. Figure 6b shows a vertical cross-section of the modeled fault plane and the surface projection of the fault is mapped in

Fig. 6a, c. Figure 6c also shows that the modelled fault fits the mainshock hypocentre location, as well. The fault's upper edge is projected to the sea-bottom near the Gulf of Gökova western ridge (Fig. 1; Fig. 6a). We then analyzed the sensitivity of the solution to the various parameters of the inversion using a systematic analysis of the parameters space (in Supplementary Fig. S4 we present the cases of fault width and amount of slip). The uncertainties listed in Table 5 make use of the results of this

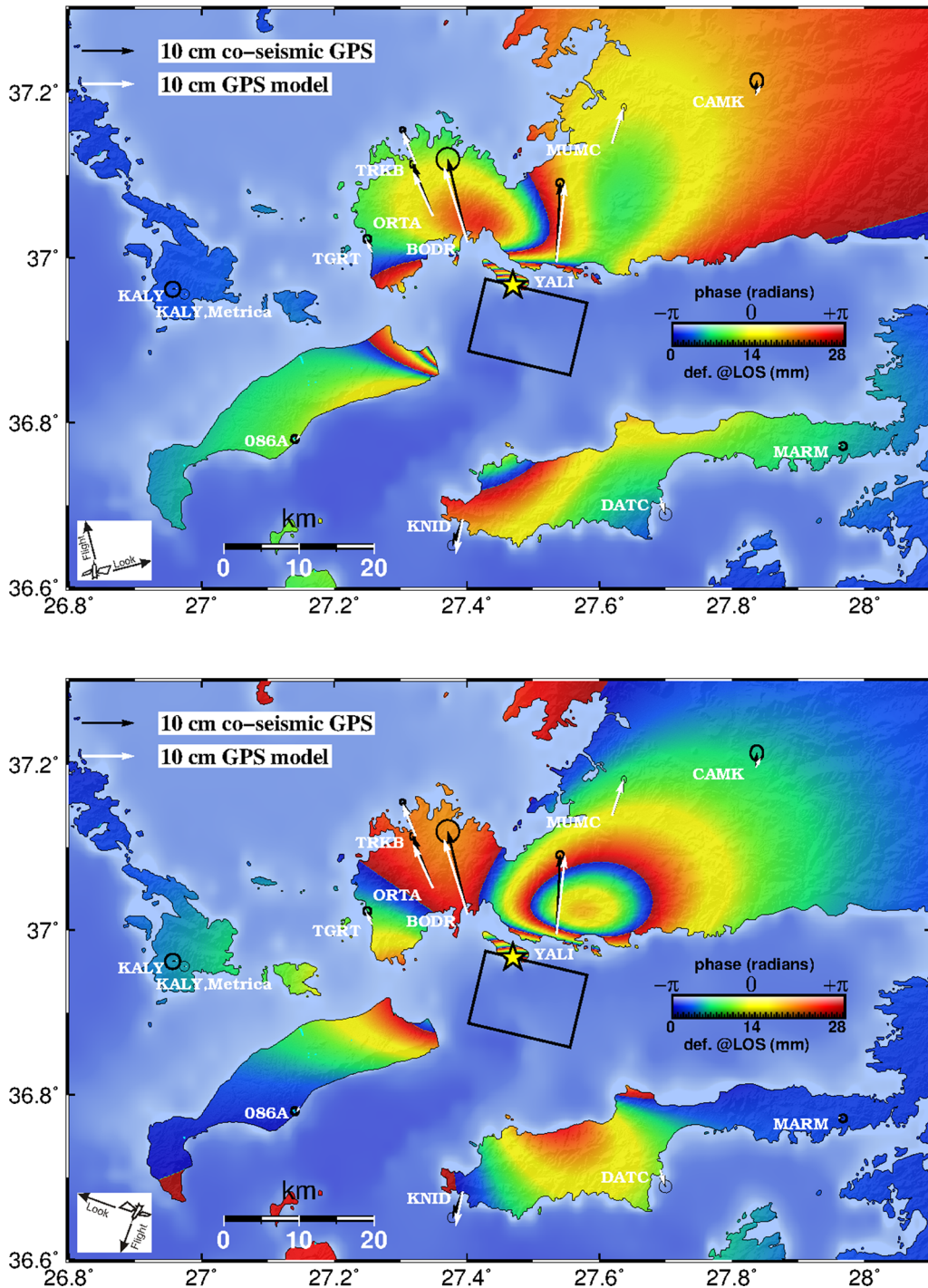


Figure 7

Synthetic interferograms from the north-dipping fault model for ascending and descending orbits (top, bottom), respectively. The inferred source for the mainshock is shown by the black rectangle (surface projection). Yellow star indicates the earthquake epicentre (relocated in this study). GNSS observed and modelled co-seismic displacements are in Table 2 and Supplementary Table S1, respectively

Table 6

Reference (NOA; based on Panagiotopoulos, 1984), Starting (Init.) and best RMS (Final) P-wave 1D velocity (V_p) models

Layer	NOA model		Init. model		Final model	
	Depth (km)	V_p (km/s)	Depth (km)	V_p (km/s)	Depth (km)	V_p (km/s)
1	0.0	5.00	0.0	5.70	0.0	4.88
2	1.5	6.00	3.5	5.90	3.0	5.81
3	18.5	6.60	23.0	6.20	11.0	6.13
4	31.0	7.90	29.0	7.40	25.0	7.63
5	–	–	32.0	7.50	40.0	7.97
6	–	–	80.0	8.20	80.0	8.20

“Depth” stands for the respective layer’s ceiling depth

analysis of the “space” of solutions. The final fault model fits the geodetic observations well (Fig. 7) as demonstrated by the patterns of synthetic interferograms for the two viewing geometries and the predicted horizontal displacements at GNSS locations (modelled using the parameters of Table 5; see supplementary Table S1), along with the actual GNSS measurements (Table 2). The fringe pattern, orientation, direction and density of the modeled interferograms match very well the real ones in Karaada islet (Fig. 4). There is a high quality of fit of all GNSS data, within observational error bars almost at all sites (Fig. 7).

To summarise this section, we list below the most important findings from the joint analysis of the GNSS & InSAR co-seismic and post-seismic interferograms:

- The best modelled fault is north-dipping, as this is constrained by the conjunction of GNSS and InSAR. Using only one of the data sets does not allow to conclude the dip-direction.
- The fault does not reach the surface; its top is at approximately 2.5 km depth.
- The bottom edge of the fault is around 10 km depth.
- The fault has a relatively low dip angle of $37^\circ \pm 3^\circ$.
- The component of rake is significant with a clear component of left-lateral motion (rake $75^\circ \pm 3^\circ$).
- The ratio slip/surface puts this earthquake in the family of events with relatively large slip with respect to the size ($M_w = 6.6$; same family as events like Bam and Christchurch for example,

Wang et al. 2004; Elliott et al. 2012). This type of rupture is usually characterized by ground accelerations above average in the epicentre area.

4. Seismicity Data and Location Procedure

4.1. Crustal Velocity Model

In this section we describe the methodology that was followed to determine the hypocentral locations of the 2017 Kos aftershock sequence. We collected parametric and waveform data from various sources (see Supplementary Text S1 for a description of seismological data) and acquired initial locations using a starting velocity model (NOA model in Table 6). An average V_p/V_s ratio of ~ 1.74 was determined using the Wadati method (Wadati 1933; Fig. 8). This is consistent with similar V_p/V_s values measured in the literature for the broader region (e.g. Sodoudi et al. 2006; Karakonstantis 2017). The VELEST algorithm (Kissling et al. 1994) was employed for the estimation of a minimum 1D velocity model, optimized for the 2017 Kos aftershock sequence and available station geometry (see Supplementary Fig. S1 for station distribution), using arrival-time data from a subset of ~ 350 events with initial RMS errors < 0.5 s, azimuthal gap $< 180^\circ$ and horizontal location errors < 2 km. A starting velocity model for the South Aegean was considered (Brüstle 2012), which was derived using data from the EGELADOS Project. For the present study, numerous tests were run for a variable number of

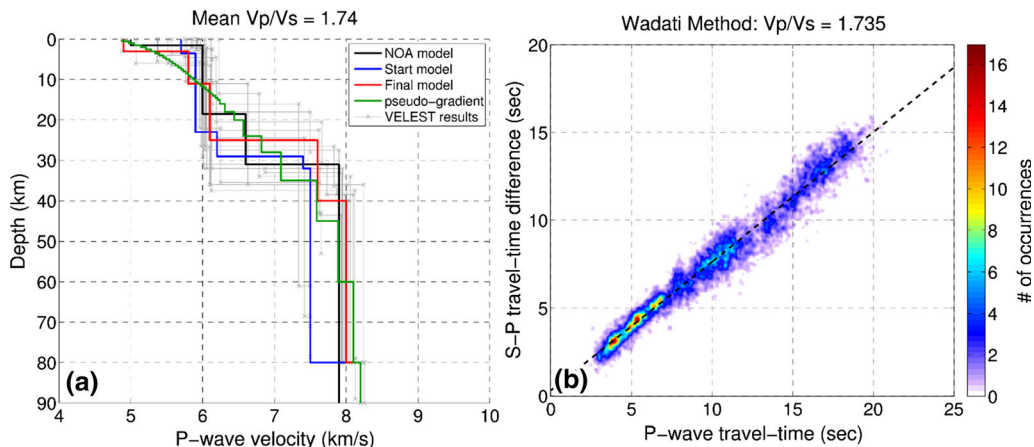


Figure 8

a Collective results of the VELEST algorithm (gray lines) for the determination of a minimum-RMS V_p model (red) from a 6-layer starting model (blue) following the procedure described in the text. The default regional model for Greece (NOA model) is displayed for comparison, along with a pseudo-gradient model that was used for the relocation procedure, **b** V_p/V_s ratio estimated using the Wadati (1933) method

layers and ceiling depths, inverting the travel-time data for the determination of velocities using VELEST. The half-space discontinuity, beneath which velocity is considered constant, was set at 80 km depth, similarly with other models of the broader area (e.g. Akyol et al. 2006; Karakonstantis 2017).

For each run with a different number of layers, 100 sets of inversions with different configurations of randomly selected layer ceiling depths were performed. Based on a 6-layer velocity model which minimized the r.m.s. residuals, an optimal model was constructed (“Final Model”; Table 6), with an additional constraint for the Aegean Moho discontinuity at a depth of 25 km, supported by geophysical studies for the broader region (e.g. Tirel et al. 2004; Sodoudi et al. 2006; Zhu et al. 2006; Grigoriadis et al. 2016). An alternative pseudo-gradient model (Fig. 8a, green line) was also considered for use during the relocation procedure, in order to reduce artifacts near the simple 6-layer model’s discontinuities, by interpolating between the mean velocities at the successive layers’ interfaces. Initial locations were resolved using the HypoInverse algorithm (Klein 1989) with a constant ratio $V_p/V_s = 1.74$. Station-corrections were then calculated and applied to the P- and S-wave travel-times and the location procedure was repeated, yielding improved results with respect to both

location residuals (Table 7; Fig. 9) and spatial dispersion (Fig. 10).

4.2. Relocation Procedure

To further improve the spatial distribution of the Kos aftershock sequence the double-difference HypoDD algorithm (Waldhauser 2001) was employed. This method works by minimizing the double-differences between observed and calculated travel-times for pairs of neighbouring events with the assumption that the roughly common ray-path length is much larger than the inter-event distance; hence any differences in the travel-times can be attributed to the latter. Minimizing these double-differences can reduce relative location residuals due to unmodeled velocity structure while cross-correlation differential times can reduce arrival-time reading errors for strongly correlated events.

Stations NISR and DAT that provided waveform data for the whole sequence (see supplementary Fig. S1 for locations; station BODT was unavailable during the first days), were selected as reference stations for the determination of multiplets. Cross-correlation, $XC(t)$, was performed for all combinations of event-pairs on all three components, on the full waveform signals (including both P and S), filtered in the range 2–15 Hz, for station NISR, and

Table 7

Event location statistics for various models. “Stat. Corr.” stands for applied station corrections to P- and S-wave travel-times

V_p model	NOA model	Starting model	Final model	Final + stat. corr.
V_p/V_s	1.74	1.74	1.74	1.74
Mean RMS (s)	0.487	0.444	0.410	0.356
Mean ERX (km)	0.669	0.618	0.614	0.506
Mean ERY (km)	0.700	0.644	0.656	0.542
Mean ERZ (km)	5.303	3.882	3.238	2.804
Mean Depth (km)	5.421	9.249	4.980	5.227

The ratio $V_p/V_s = 1.74$, was calculated using the Wadati (1933) method. Number of events is 1123

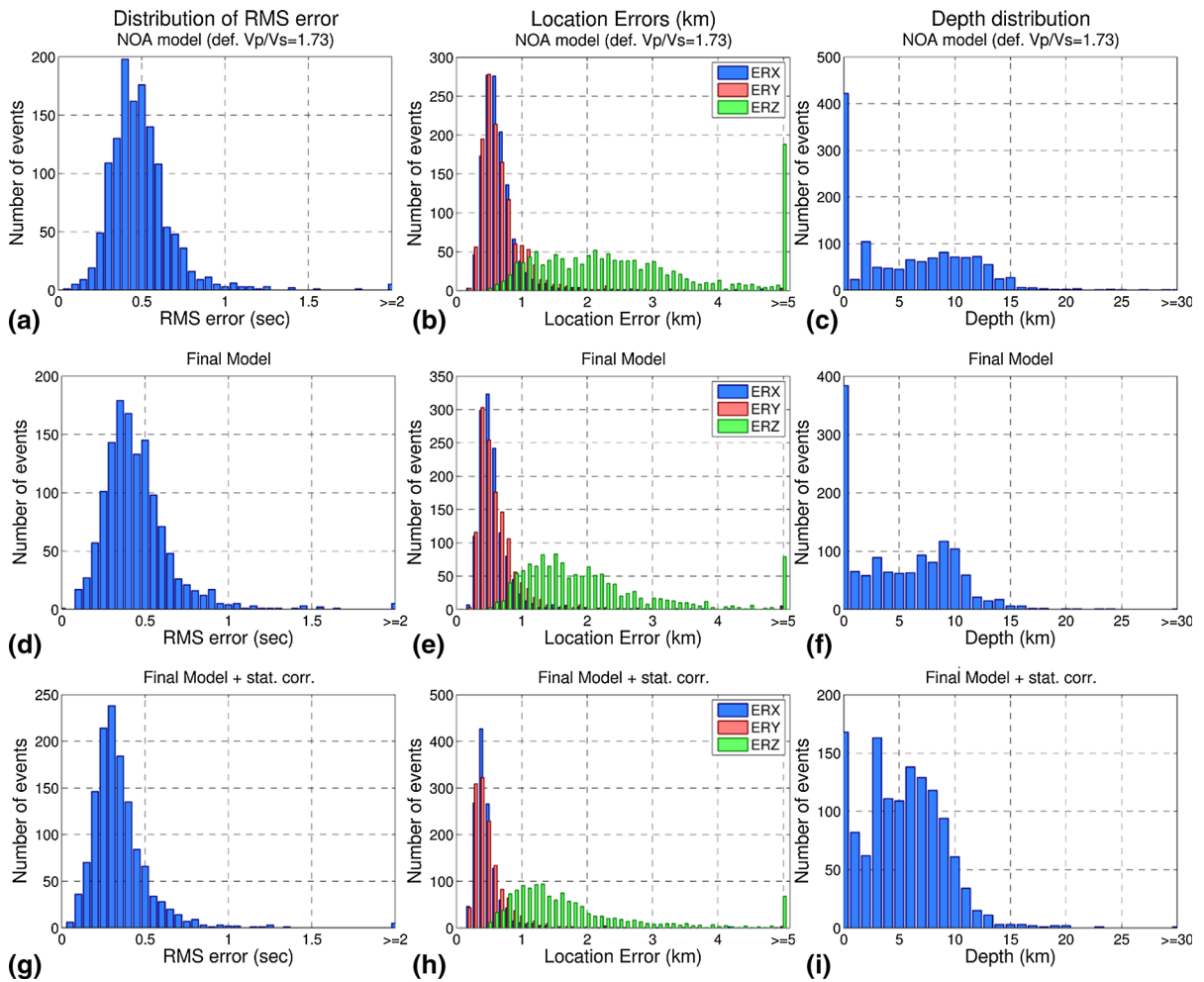


Figure 9

Distribution of r.m.s. errors (a, d, g), location errors (b, e, h) and focal depths (c, f, i) for the 2017 Kos aftershock sequence using the default velocity model for Greece (a–c), the minimum-RMS 1-D model determined by VELEST (d–f) and the latter after application of station corrections (g–i), respectively

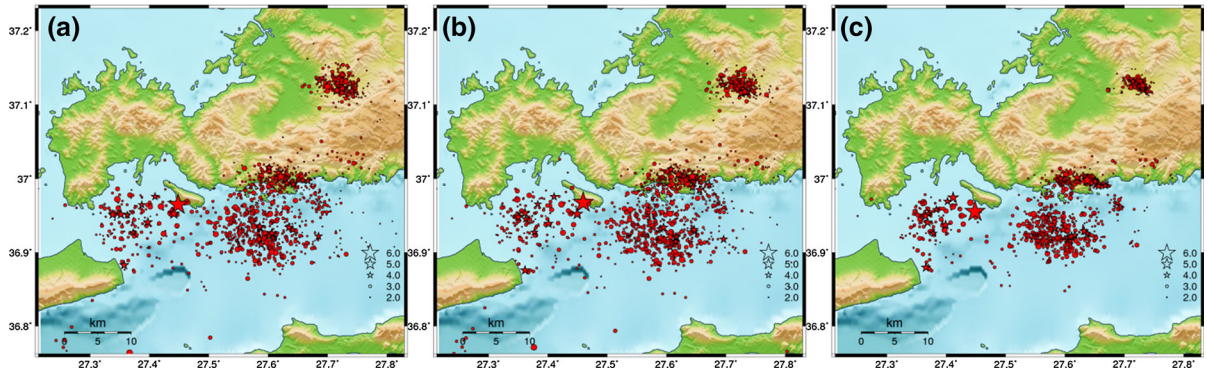


Figure 10

Epicentres of the 2017 Kos earthquake sequence, **a** initial locations using the “Final Model” (Table 6), **b** locations after the application of station corrections and **c** relocated with HypoDD using the pseudo-gradient model (Fig. 8a)

2–8 Hz, for station DAT (due to a lower sampling rate of 20 sps), respectively. The maximum value $XC_{\max} = XC(t_m)$ of any component for each pair was registered into a correlation matrix. Nearest-neighbor linkage was applied and an optimal threshold value, $C_{th} = 0.61$, was selected by employing an empirical rule to maximize the difference between the size of the largest cluster and the sum of clustered events (Kapetanidis 2017). As a result, a total of 810 events were contained in 122 multiplets that were formed.

For all event-pairs within each multiplet, cross-correlation of P- and S-waves was then performed separately on each of the 6 closest stations, after proper temporal alignment to the respective observed arrival-times, registering both t_m (differential time; equivalent to the time-lag that maximizes the XC function) and XC_{\max} (observation weight) values to be used as cross-correlation data for HypoDD. Relocation was performed, using the pseudo-gradient V_P model (Fig. 8a) a constant ratio of $V_P/V_S = 1.74$, and the station-corrected hypocentres as initial locations to facilitate the linkage procedure. The inversion was run by applying low a priori weights to the cross-correlation data and high weights to the catalogue data during the first iterations. The reverse relation was then applied to the last sets of iterations to improve relative locations between strongly correlated events.

Despite the poor network coverage of the area, the relocation procedure managed to increase the clarity of the spatial distribution, at least as far as the epicentres are concerned (Fig. 10c). To further

improve the results, the relocation was repeated on subsets of spatial groups (or clusters) that could already be discriminated in the preliminary solutions. The relocated epicentre of the mainshock is 36.9553°N , 27.4484°E (depth at $9.2 \text{ km} \pm 0.5 \text{ km}$). The relocated catalogue is available as supplementary material to this study (1123 events). We also observe that most of the relocated aftershocks are located away from the mainshock epicentre and toward both edges of the fault plane, forming several clusters (Fig. 10). This suggests that the main fault plane may have ruptured as in one asperity with a few unbroken patches (if any).

4.3. Spatial Analysis of Aftershocks

To further analyse the results of the relocated catalogue, the 3D spatial distribution was divided into six (6) groups-clusters (Figs. 11, 12) by employing Ward’s linkage (Ward 1963) on the matrix of inter-event hypocentral distances using an appropriate threshold. Two significant clusters, #1 and #3, are horizontally separated by a 15-km gap which roughly delineates the area of the main rupture that is nearly void of aftershocks. The occurrence of few aftershocks towards the middle of the fault plane (Fig. 12, section c1-c2) confirms that this area of the fault plane experienced high-slip while the majority of the aftershocks are distributed on low-slip areas towards both ends of the rupture (Das and Henry 2003; Melgar et al. 2017; Feng et al. 2017). The western cluster (#1) is composed of significantly less events

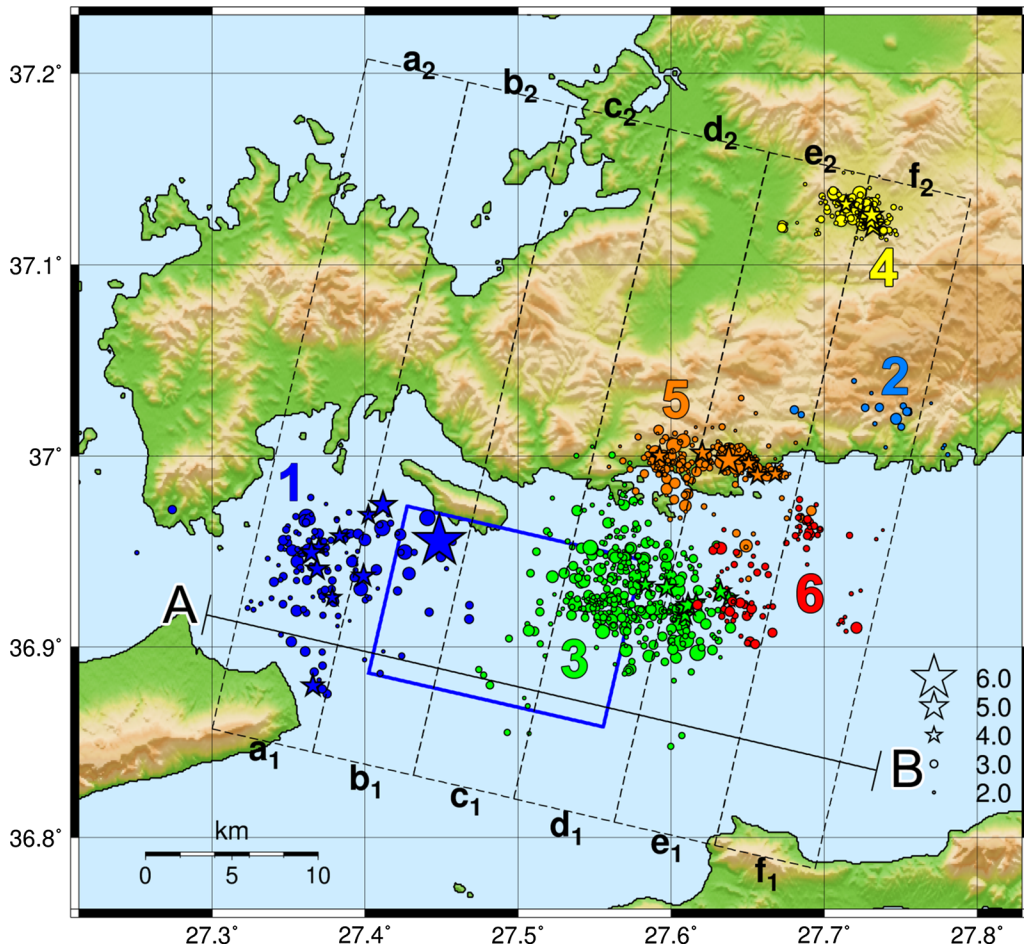


Figure 11

Relocated epicentres of the 2017 Kos earthquake separated in six (6) spatial groups (1–6). Dashed rectangles mark the bounds of the parallel N13°E cross-sections of Fig. 12. The N103°E oriented profile line A–B is used for the spatiotemporal projection of Fig. 15. The blue rectangle represents the projection of the fault plane that was constrained by geodetic data

than the eastern one (#3). Cluster #5, slightly north of #3, consists of two densely packed sub-clusters, oriented almost E-W. Cluster #6 also contains a small sub-cluster of correlated events, slightly SE of the eastern sub-cluster of cluster #5 and a few other sparse events that may relate to cluster #3. Finally, cluster #4 is a dense cluster that was activated during the Kos sequence but is much separated, about 25 km NE of the rupture plane. Cluster #2, also oriented E-W, occurs slightly ENE of Group #5, consists of few events and will not be discussed any further.

The hypocentral depth distribution has been generally problematic, due to the lack of available local seismological stations in the area that could help

to better constrain it. The hypocentral depths mainly range between 3 and 10 km, but several clusters are distributed roughly sub-vertically, as can be seen in a series of parallel cross-sections (Fig. 12). However, the western cluster #1, in particular, appears to deepen towards the north (Fig. 11a1–a2, b1–b2), although its distribution is not strictly planar. This pattern agrees with the fault model determined from geodetic data, which confirms that the mainshock ruptured a north-dipping fault (Fig. 6). The dip angle ($\sim 37\text{--}40^\circ$) indicated by the hypocentral distribution of Cluster #1 also appears to be compatible with the north-dipping nodal plane of the mainshock's focal mechanism. The northeastern clusters (#4 & #5) also

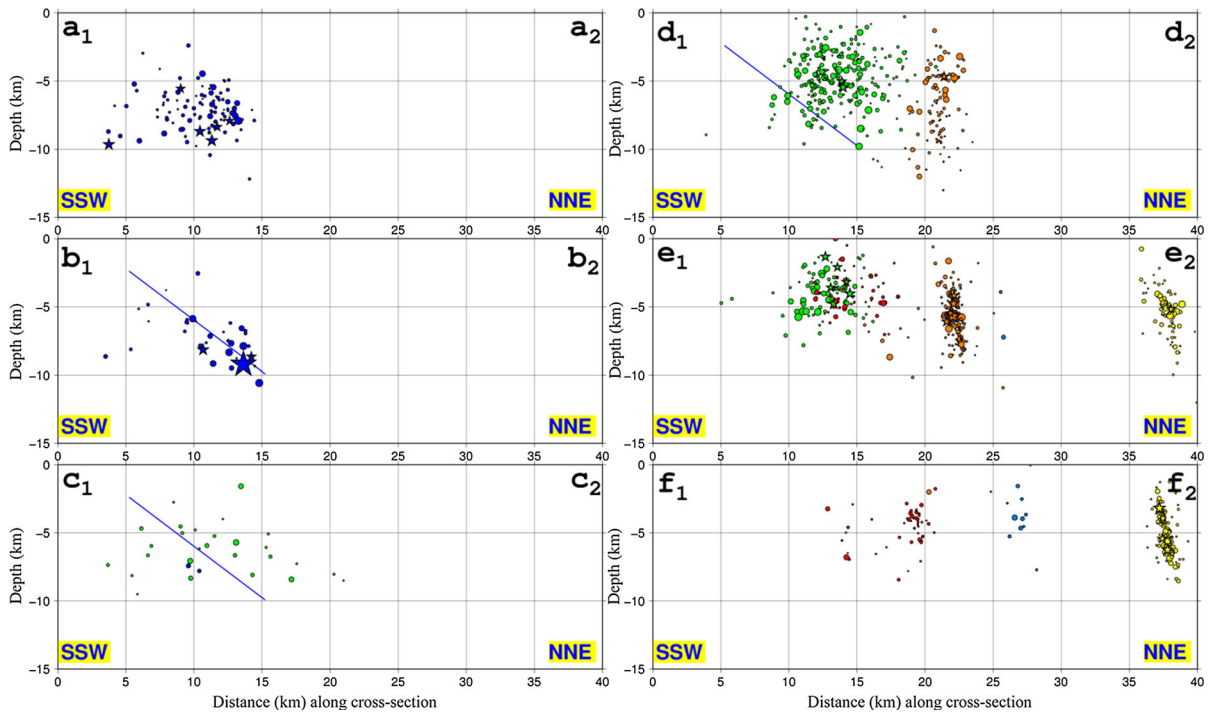


Figure 12

Series of N13°E-oriented, 6 km-wide parallel cross-sections a–f (see Fig. 11) for the relocated hypocentres of the 2017 Kos earthquake sequence. Diagrams are down to 15 km depth. Colors represent the six (6) spatial groups (clusters) defined in Fig. 11. The 37° N-dipping blue line in cross-sections b1–b2 & c1–c2 & d1–d2 corresponds to the projected rupture plane, as determined by geodetic data. The aftershock depth distribution indicates no offset between north-dipping model and hypocentres

follow north-dipping planes (Fig. 12; sections e1-e2 & f1-f2) that do not correlate with any of the fault sources from the SHARE database (Gürer and Yılmaz 2002; Ulug et al. 2005). However, we repeat that the focal depths are poorly constrained due to the lack of arrival-time data from local stations.

5. Stress Transfer Modelling

Static stress changes due to the mainshock have been computed on receiver faults using the Coulomb failure criterion (King et al. 1994; Ganas et al. 2006; Toda et al. 2011), assuming the source parameters listed in Table 5, effective coefficient of friction $\mu' = 0.4$ and N–S regional extension. Most receiver faults in the Kos-Bodrum area strike $\pm 30^\circ$ with respect to the seismic fault (Fig. 1) so it is reasonable to model static stress transfer on faults with similar kinematics as that of the 20 July 2017 mainshock, but

also on faults optimally oriented to the regional stress field. As in Sect. 3, we assume that failure of the crust occurs by shear so that the mechanics of the process can be approximated by the Okada (1992) expressions for the displacement and strain fields due to a finite rectangular source in an elastic, homogeneous, and isotropic half-space. The result presented in Fig. 13 (at depth of 7 km) shows (a) positive stress changes (loading) along strike of the seismic fault of the order of several bar and (b) negative stress changes (stress shadows) across the fault, therefore it is suggested that this stress transfer model explains well the marginally on- and mainly off-plane distribution of aftershocks at that depth. The Coulomb stress change model was also examined in cross-sections oriented N13°E, perpendicular to the 20 July 2017 rupture, to examine its distribution with respect to the relocated hypocentres (Fig. 14).

The western cluster #1, which is the one related more directly to the mainshock's fault plane, is

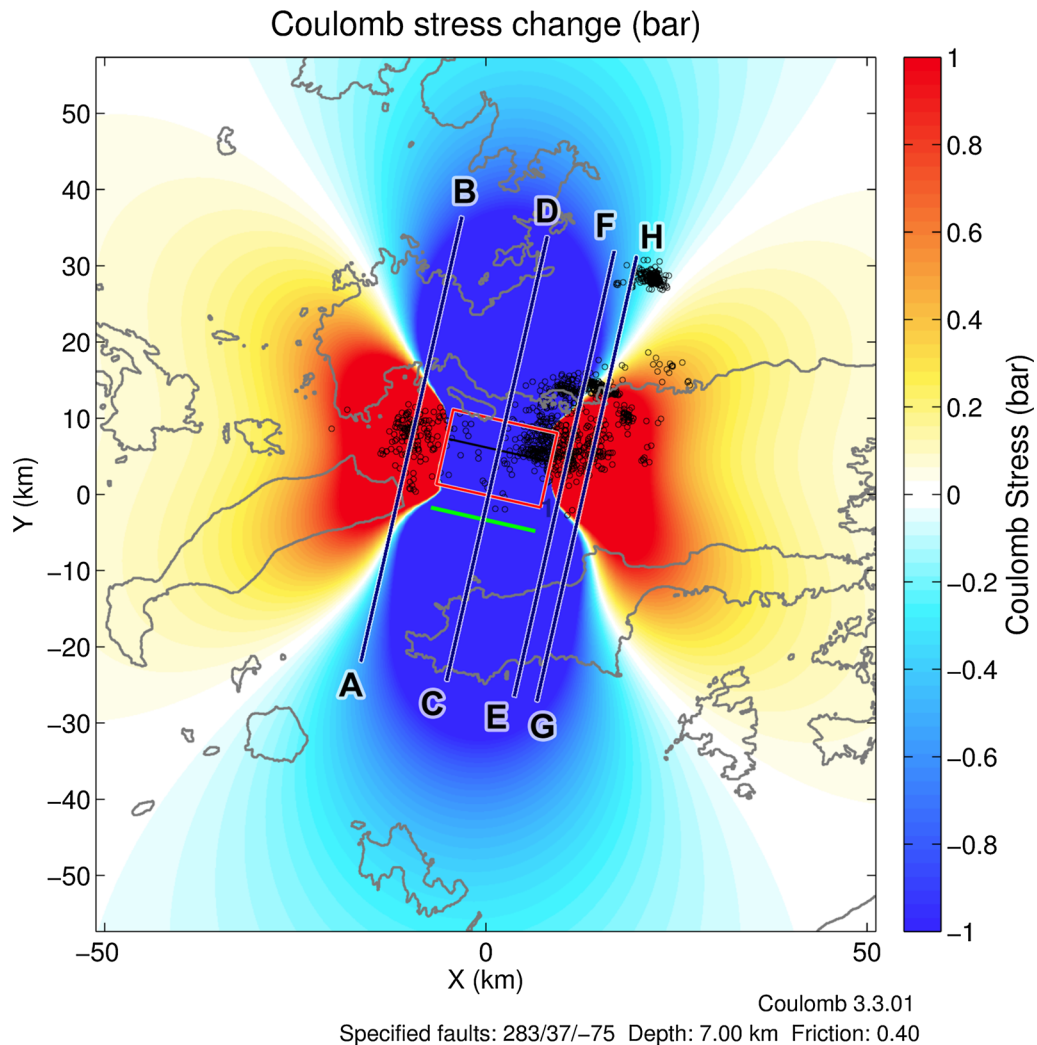


Figure 13

Coulomb stress changes at 7-km depth associated with the July 20, 2017, 22:31 UTC Mw = 6.6 earthquake. The palette of Coulomb stress values is linear in the range -1 to $+1$ bar. The stress change has been computed for receiver faults with the same kinematics as the source model (strike/dip/rake = $283^{\circ}/37^{\circ}/-75^{\circ}$; see Table 5). Red rectangle is the surface projection of the rupture plane, and green line is its surface trace (projected up-dip). Open circles are relocated aftershocks for the period of 20 July–20 August 2017. Color scale in bar (1 bar = 0.1 MPa); blue areas: unloading (relaxed); red areas: loading. The N13°E oriented cross-sections are presented in Fig. 14. More slices at different crustal depths are shown in Supplementary Fig. S5

completely within the loaded area, which is consistent with both the fault model and the Coulomb stress transfer for receiver faults of the same type. This stress loading pattern holds for all modelled depths (5 km, 7 km, 9 km and 11 km; see the maps in Supplementary Fig. S5). Two aftershock clusters (cluster #3 and cluster #5; Fig. 11) are half-inside the loaded area (Figs. 13, 14), while clusters #2 and #6 are totally inside the $+0.1$ to $+1.0$ bar lobe

(Fig. 13). For the case of the largest aftershock of 8 August 2017 07:42:21 UTC, two Coulomb models were examined, one for each of the nodal planes of its focal mechanism as the receiver fault (Supplementary Fig. S6). According to the NOA focal mechanism for this event http://bbnet.gein.noa.gr/mt_solution/2017/170808_07_42_21.89_MTsol.html (last accessed 2 June 2018) the two nodal planes suggest either a WNW-ESE fault, dipping at 64° towards NNE, or a

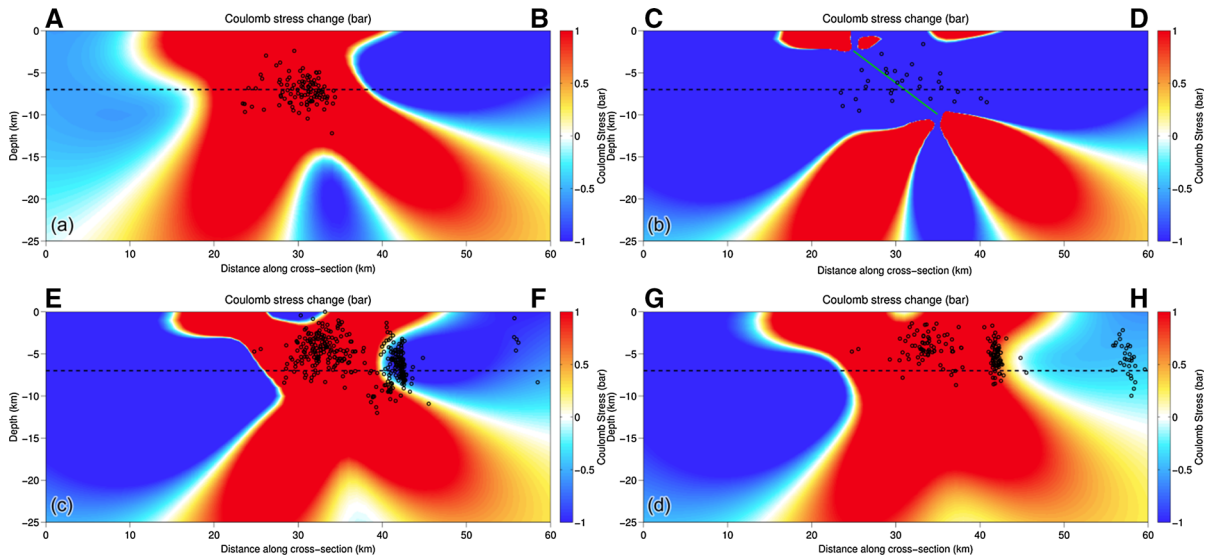


Figure 14

Parallel, vertical cross-sections in a N13°E direction, perpendicular to the July 20, 2017 seismic fault, along the profile lines of Fig. 13 for the same Coulomb stress change model, crossing, **a** cluster #1, west of the fault (A-B), **b** the fault's centroid (C-D), **c**, **d** east of the fault, including clusters #5 of the largest aftershock and #4 of the isolated northern cluster (Fig. 11). Thick cyan line (inclined towards the north) in panel **b** indicates the modelled fault plane. The black dashed horizontal line depicts the map slice of the Coulomb stress distribution shown in Fig. 13. Black circles are the relocated aftershocks for the period 20 July–20 August 2017, selected in slices of ± 2 km width on either side of each cross-section's plane

WSW-ENE fault, dipping towards SSE (strike = 62° , dip = 36° , rake = -132°). It is found that for the south-dipping plane, the Coulomb stress model at depths of 5 and 7 km (Supplementary Fig. S6) favours loading of eastern half of Cluster #5, where the $M_w = 5.2$ event occurred. Since the cluster's spatial distribution is mainly subvertical, with large uncertainties at depth, an antithetic, south-dipping fault could be plausible, as far as the triggering mechanism is concerned. However, when considering receiver faults optimally oriented to the N–S extensional stress field, this sub-cluster, along with most of the other aftershocks, is within the loaded zone of the mainshock (Supplementary Fig. S7). In others words, based on Coulomb-stress modelling we cannot conclude which nodal plane was activated.

Cluster #4 was activated on 13 August 2017 after a $M_w = 4.9$ event (25 km NNE of the epicentre) so it was most probably the result of static stress transfer caused by the mainshock; however, in our uniform-slip model for the mainshock it appears to be inside a Coulomb stress shadow (Fig. 13). This is due to cluster #4 being activated because of either delayed

dynamic triggering (Parsons 2005) or the triggered aftershocks occurred on faults with a geometry different than the mainshock. Indeed, if we compute stress changes on faults optimally oriented to regional extension (Supplementary Fig. S7) this cluster is included within the loaded area, so it seems reasonable to accept this hypothesis. In Fig. 12, section f1–f2 the cluster #4 aftershocks are aligned along a near-vertical fault plane; therefore, it is concluded that a high-angle geometry is more compatible with Coulomb-stress triggering of those events.

The four cross-sections across the Coulomb failure model (Fig. 14) present the relocated aftershock distribution towards both ends and below the rupture and indicate that the fault probably ruptured as one asperity. We observe that most of the modelled fault plane is void of aftershocks except for its eastern side, while it is surrounded by loaded areas at the edges of the main rupture (see also Supplementary Fig. S5). We also note that triggered seismicity (period July 20–August 20, 2018) is restricted within less-than-one fault length of the main rupture, except for cluster #4.

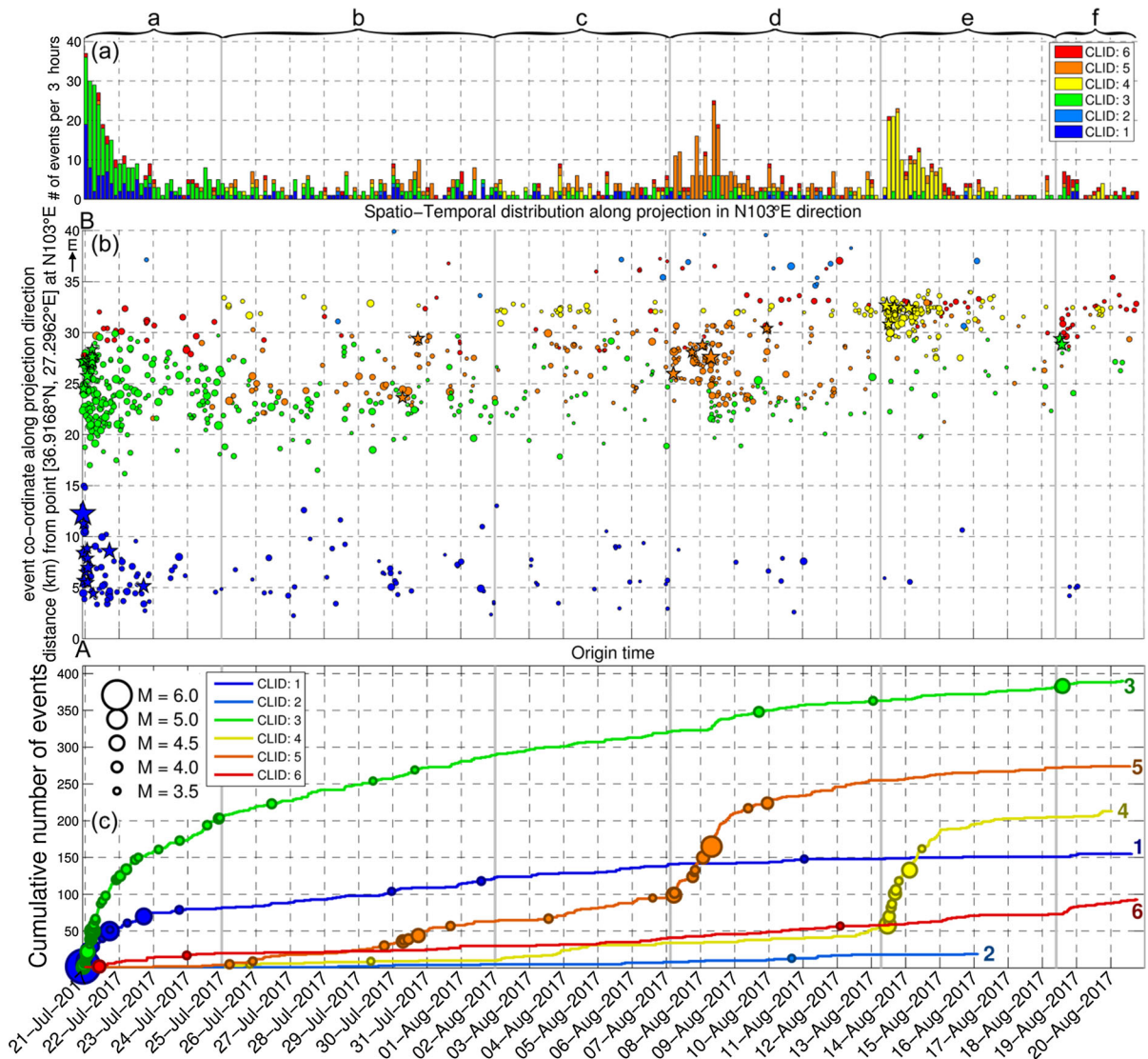


Figure 15

Spatiotemporal projection of relocated seismicity along a N103°E direction **a** Histogram of the number of earthquakes of the 2017 Kos sequence per 3 h, stacked per spatial group (CLID #), **b** spatiotemporal projection of the relocated epicentres along the N103°E oriented profile A-B in Fig. 11. Stars represent earthquakes with $M \geq 4.0$. **c** Cumulative number of events for each of the 6 spatial groups. Circles in **c** denote the larger events ($M \geq 3.5$). Vertical thick gray lines divide the 6 successive temporal periods (labels a-f at the top)

6. Discussion

6.1. Spatiotemporal Evolution of Seismicity

To visualize the temporal evolution of the aftershock sequence, its spatiotemporal projection was performed in a N103°E direction (Fig. 15), along with a division into six (6) temporal periods (Fig. 16). As soon as the mainshock occurred, seismicity

quickly spread along both clusters #1 and #3, in a total length of ~ 24 km. Although cluster #1 includes the mainshock and some major aftershocks that occurred during the first days, most of the aftershock activity took place in cluster #3 which is also the most populated one (a factor of 3 more than cluster #1; Fig. 15) and includes a large number of moderate events. Most of cluster #1 & #3 aftershocks

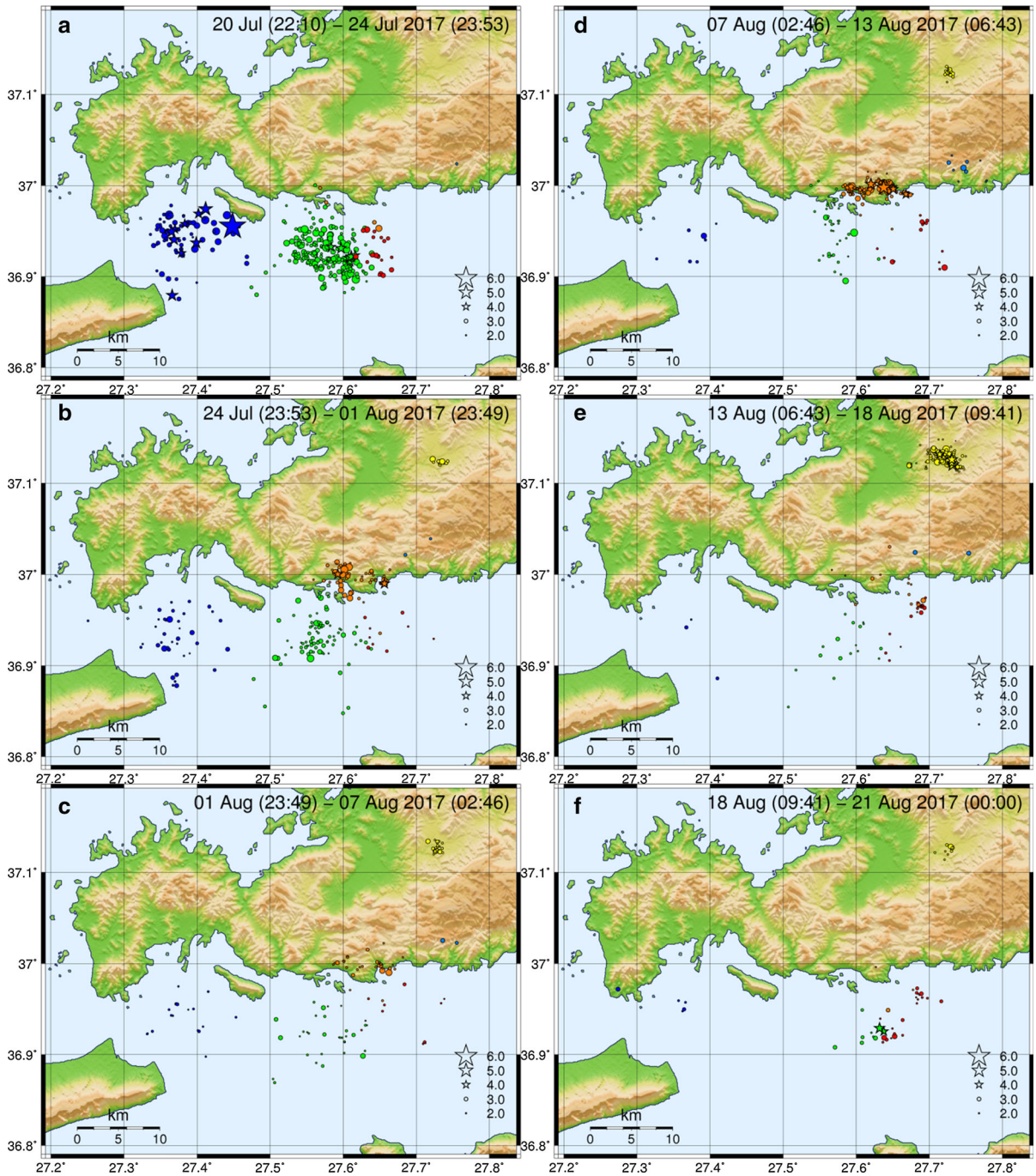


Figure 16

a Maps of the relocated epicentres of the 2017 Kos earthquake sequence, divided in 6-time periods (**a-f**; Fig. 15; 20 July 2017 upper left, 20 August 2017 lower right). Colours represent the 6 spatial groups (clusters)

occurred within 4-days of the mainshock. Some activity in clusters #2, #5 and #6 also started to appear after 25 July 2017 while a low rate of

seismicity was observed in cluster #2 and #6. On 7 August 2017, a significant outburst started in cluster #5, following an $M_L = 4.5$ event. It culminated on 8

August 2017 07:42:21 UTC in the largest aftershock of the sequence, an $M_w = 5.2$ earthquake, which also triggered some activity in cluster #3. The WSW-ENE trending nodal plane could possibly match a south-dipping fault (Fig. 1), but the dip-angle (36°) is low while that geometry would make the “inferred” normal fault to outcrop further inland. On the other hand, the WNW-ESE trending plane, dipping at 64° towards NNE fits with the north-facing, near-vertical distribution of aftershocks (seen Fig. 12, section e1–e2; cluster 5). The activity at cluster #5 began to diminish after 9 August 2017.

At the isolated, northern cluster #4, which had been presenting signs of activity since 25 July 2017, an outburst occurred on 13 and 14 August 2017, following two moderate events with $M_w = 4.9$ and $M_w = 4.8$, respectively. We stopped our analysis on 20 August 2017 (1 month after the mainshock) as aftershock decay patterns appeared normal (Fig. 15). No large aftershock occurred after that date.

In summary, the spatiotemporal analysis of the Kos sequence shows the following:

1. There is an absence of seismicity within the main rupture area (suggesting the rupture of one, big asperity), with aftershocks mainly at its western (Cluster #1) and eastern (Cluster #3) margins due to stress redistribution.
2. The major aftershock (8 August 2017) activated another cluster (Cluster #5) slightly to the north of Cluster #3, associated to a different normal fault (probably north-dipping).
3. It is observed a tendency of spatiotemporal migration towards the east, as seismicity in the west (Cluster #1) drops more rapidly while seismicity in the east persists for longer (including an outburst caused by the major aftershock).
4. No signs of vertical (depth) migration could be observed among clusters, likely due to limitations in the vertical resolution of the hypocentres.

In relation to the Coulomb stress change analysis (Sect. 5) it should be noted that the (co-seismic) redistribution of tectonic stress due to the July 20, 2017 mainshock is not the only factor triggering the aftershock activity, as major aftershocks and consequent sequences are also observed. This suggests that post-seismic evolution may not be described by a

simple Omori’s law, but rather by a more complex model, e.g. the ETAS (Epidemic Type Aftershock Sequence) model. However, this analysis is outside the scope of the present paper.

6.2. Limitations of the Fault Modeling Approach

Our low-angle slip model (Fig. 6) favors a normal-slip mechanism for the Kos earthquake with a minor component of left-lateral slip. The slip vector orientation is nearly N–S as expected for the Gulf of Gökova on the basis of geology (mapped active faults), seismology (mostly extensional beach balls can be seen in Fig. 2) and geodesy (strain rate pattern inverted from GNSS velocity vectors). Other important parameters of the fault model include the extent of the ruptured area ($14 \times 12.5 \text{ km}^2$) and the obtained uniform slip (2.03 m). According to Wells and Coppersmith (1994) empirical relations, the slip value is unusually large for a $M_w = 6.6$ earthquake implying that a strong asperity was involved in the rupture process.

Regarding the location of aftershocks with respect to the mainshock hypocentre (Figs. 11, 12) and their nature (i.e. on-fault or off-fault) we note that there is always a problem of poor constraint on focal depths due to the lack of data from local seismic stations. Using phases only from regional stations has the tendency to locate the seismicity deeper. This question was addressed by using a custom velocity model with a Moho depth at 25 km, constrained by geophysical data from the literature, and then applying station-corrections, as is apparent from the histograms of the depth distribution (Fig. 9). However, as biases occur, the accuracy of the hypocentral location-relocation methodology strongly depends on the available dataset and is -moreover- largely controlled by the assumed uniform velocity model which laterally varies across the region. We can, thus, consider that the “true” hypocentral depths may be offset from the resolved ones towards somewhat deeper values (although not larger than 2 km).

At the same time, we know that the homogeneous elastic modelling has the tendency to shift the modelled faults higher inside the upper crust, typically by 1–2 km (e.g. Cattin et al. 1999), the mechanical reason being that the uppermost crust is

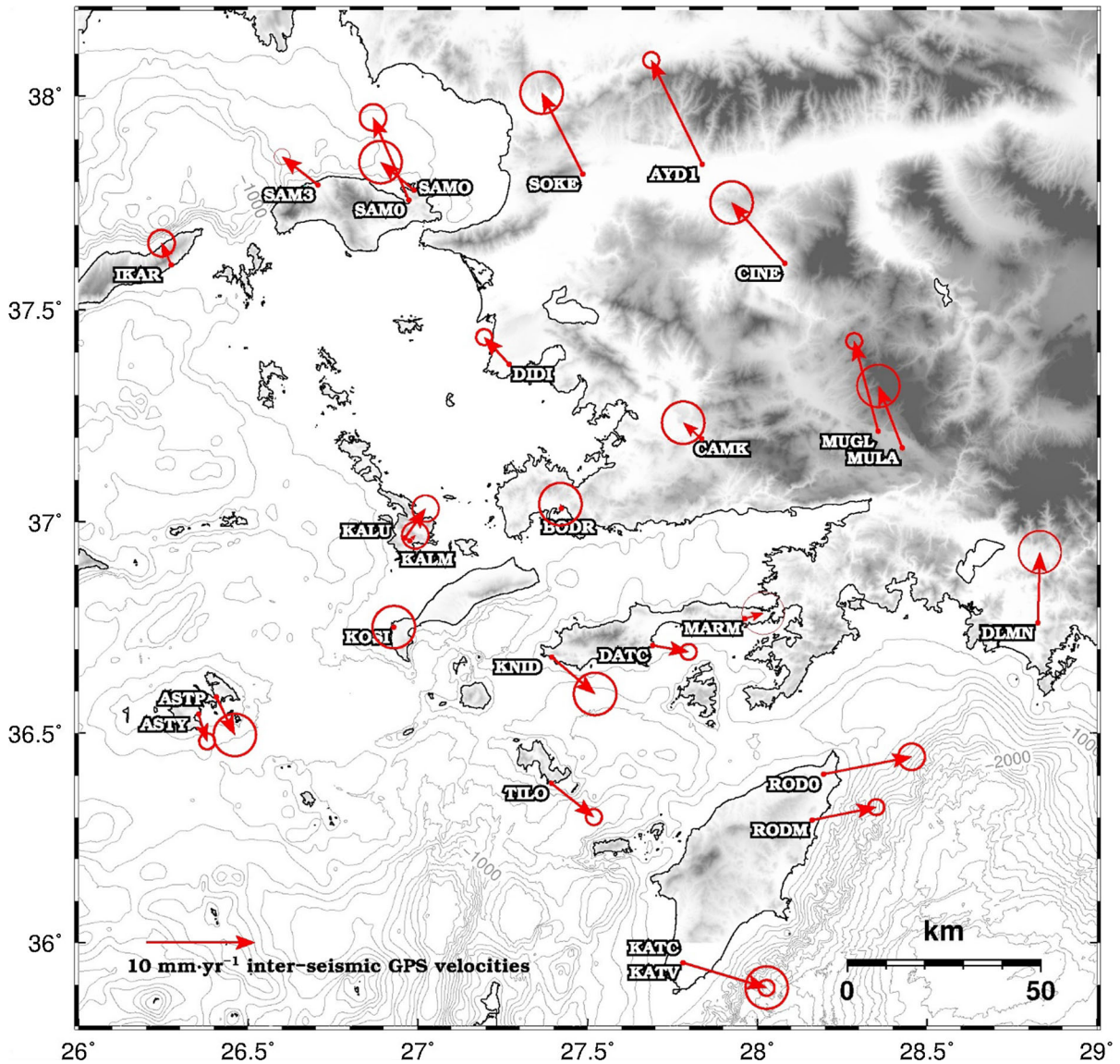


Figure 17

Map of SE Aegean showing tectonic velocities of GNSS stations with 95% confidence ellipses near the 2017 epicentral area. A counter-clockwise rotation of $3.8 \pm 0.5^\circ/\text{Myr}$ is obtained. Vectors are plotted using western Kos (KOSI station) as reference point. The velocity data is available as Supplementary Table S4

not purely elastic in fact, and it just replicates the deformation that is imposed below it. So most probably the “real” location of both fault and seismicity could be slightly deeper, with the fault plane ending at 11 km depth while seismicity may occur ~ 1 km deeper than what is shown in Fig. 12.

Lastly it has to be reminded that here we make the hypothesis of uniform slip on a rectangular fault. If

the slip is not uniform, which is most probably the case (with slip amount becoming lower towards the edges of the fault), the size of the rupture will be slightly larger. However, as the fit with the available data set is already good, we have not attempted to resolve for non-uniform slip.

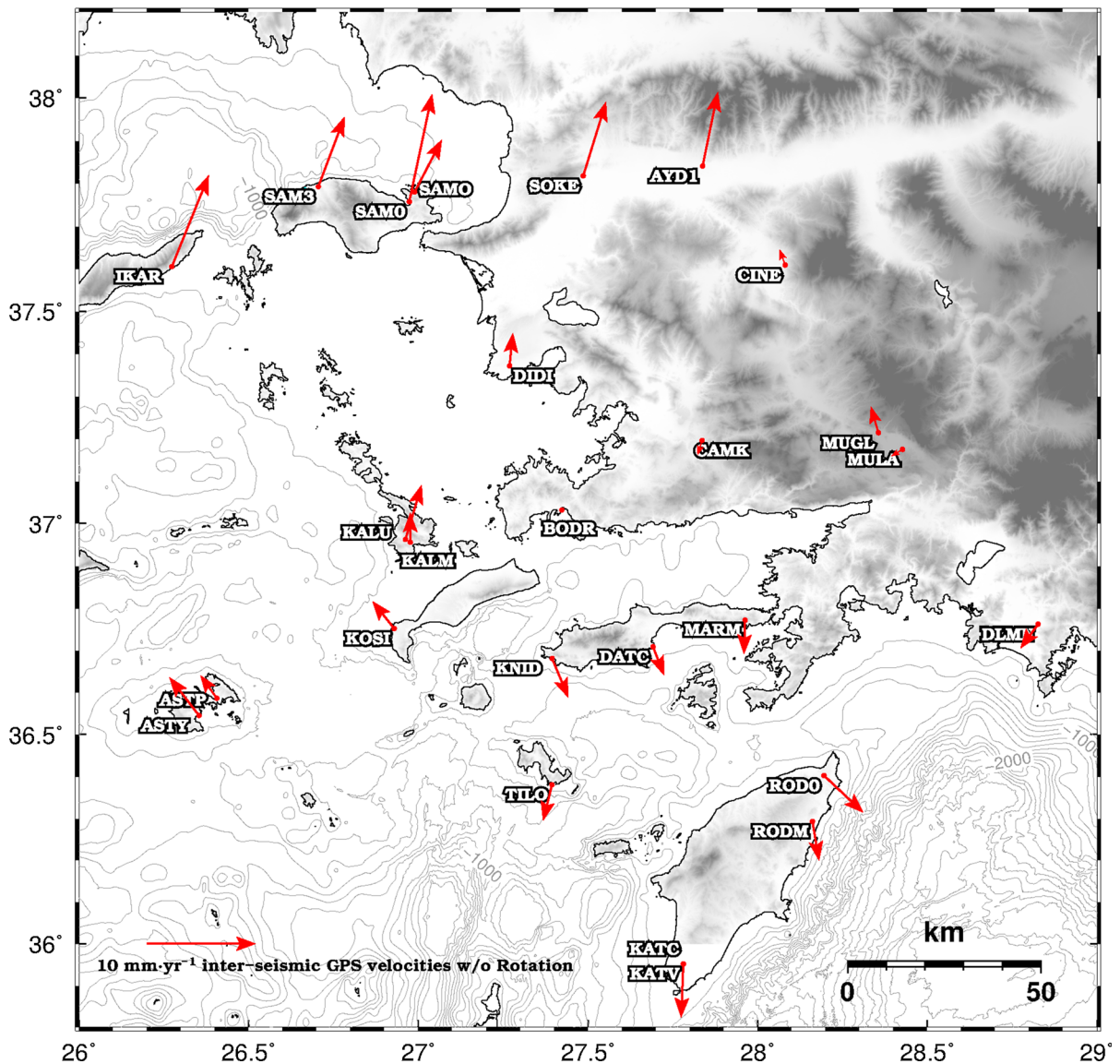


Figure 18

Map of SE Aegean showing tectonic velocities of GNSS stations near the 2017 epicentral area. Vectors are plotted after removing the rotation effect. An extension of 3.2 mm/year across the Gökova rift (along an azimuth N165°E) is obtained

6.3. Estimation of Extension Across the Gökova Rift

We estimated the “interseismic” velocities in the SE Aegean area by using observations, position time series and velocity vectors from three sources: (a) our own processing (with GIPSY 6.4) for four stations (SAMO, IKAR, KALY & RODO; period 2015–2018) provided to us by Greek private networks, (b) time series from the University of Nevada

Reno (UNR; 13 stations; <http://geodesy.unr.edu/index.php>; Blewitt et al. 2018), and c) vectors at twelve (12) campaign points of Reilinger et al. (2006). The UNR velocity estimates were obtained after analysing the average scatter of the time series in a linear regression. The campaign stations are consistent and well aligned to nearby-permanent stations, for example the stations in south Rhodes

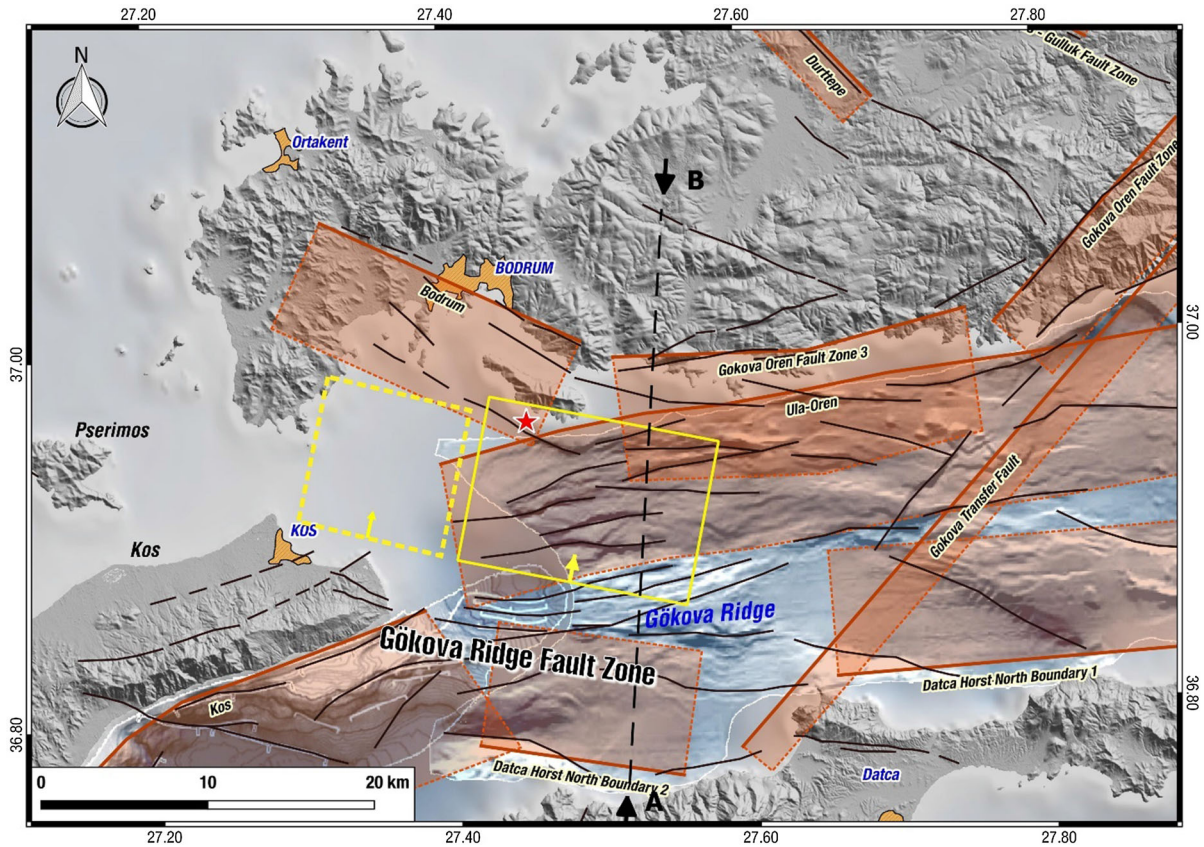


Figure 19

Tectonic map showing fault sources at the western end of the Gökova Gulf, SE Aegean Sea: Yellow rectangle corresponds to 2017 earthquake modelled fault plane accommodating a roughly N-S extension with a left-lateral component; Its possible extension towards the west (Kos fault) is also highlighted in the dashed yellow box. Yellow arrows indicate dip-direction. Red star indicates the relocated epicentre of the main shock. Fault sources from SHARE & GreDaSS (Caputo and Pavlides 2013, Basili et al. 2013) are shown as transparent orange polygons, with a thick line on surface trace projection. Profile AB displaying projected traces of the main active structures is shown in Fig. 20

KATC and KATV. The estimated velocities are listed in Supplementary Table S4 and plotted in Fig. 17.

The first clear feature in Fig. 17 is the fact that, from the point of view of an observer located in Kos, the stations located further south and east (on the edge of the Anatolian block) are rotating. Considering the rotation that minimises the residuals (L1 norm) at five points CAMK, DLMN, MULE, MUGL, CINE, this rotation is $3.8 \pm 0.5^\circ/\text{Myr}$, counter-clockwise (CCW). In other words, we used here as reference (stable) block the northern coast of the Gökova gulf, and we calculated the best fitting rotation of a southern block to which are attached the points located on that block (such as RODO, TILO etc.; see Fig. 17). Previous work by Papanikolaou and

Royden (2007) and Reilinger et al. (2010) had detected CCW rotations in SE Aegean–SW Anatolia and Howell et al. (2017) estimated that the rate of CCW rotations ranges between 0.5 and $2^\circ/\text{Myr}$ and it increases from west to east along the Gökova rift.

To estimate the rate of widening (rate of extension) of the Gökova gulf we correct all stations for this rotation (which minimizes the internal movement of the area BODR, CAMK, MUGL, MULA) and analyse the residual values at the three stations MARM, DATC and KNID (Fig. 18). We used -arbitrarily- the Bodrum region as centre for this map, just because it is close to the “centre” of the deformation, i.e. the 2017 earthquake. Then, with respect to a “stable” northern coast of the Gökova

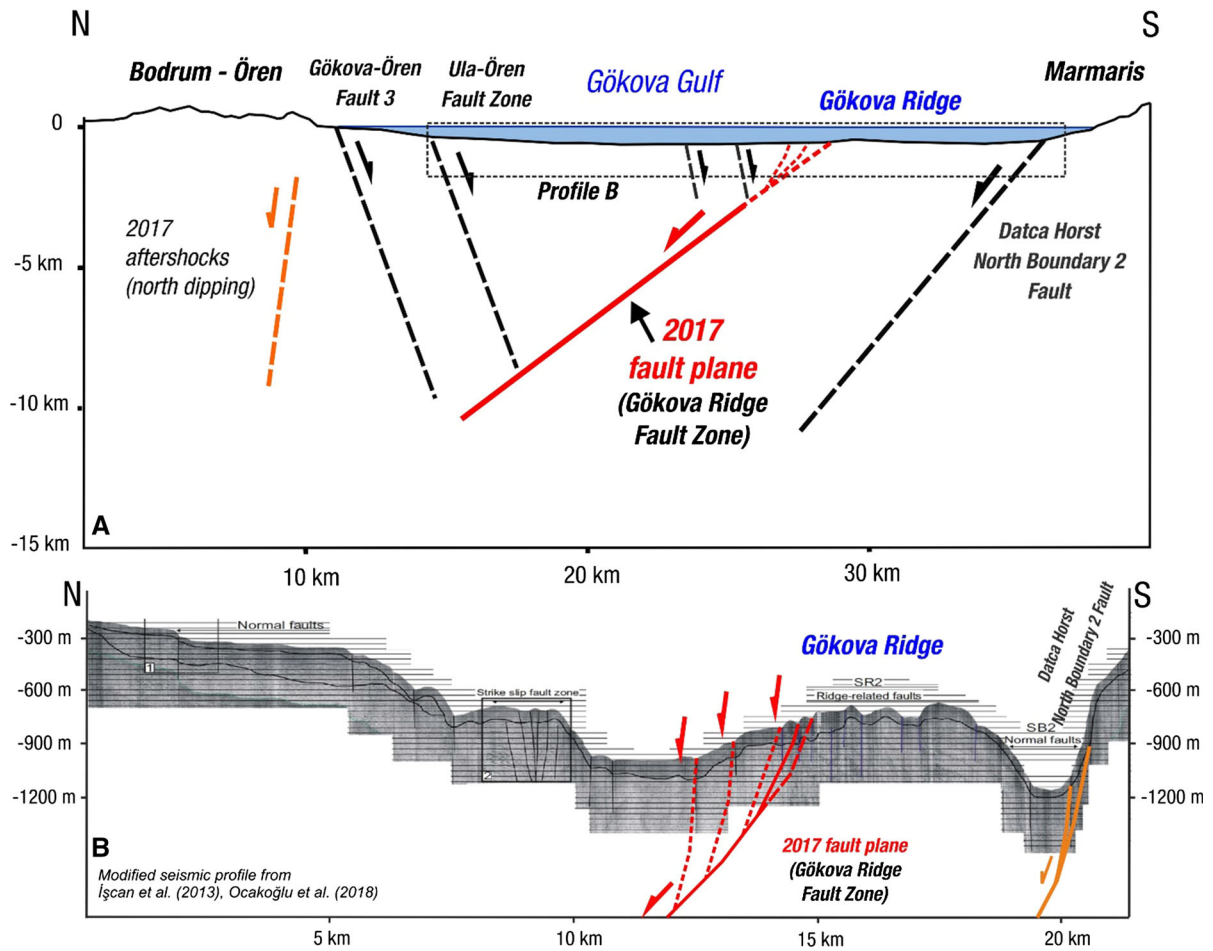


Figure 20

Cross section showing the 2017 seismic fault tectonic interpretation (a) including fault data from shallow seismic campaigns (b). Dotted polygon in Section a marks the approximate location of seismic profile b (modified from İşcan et al. 2013 and Ocakoğlu et al. 2018). Profile B shows splay (normal) faults near the surface as we interpret this structure to be the possible surface extension of the seismic fault

gulf, those three points (stations) have the following velocity vectors: MARM $-0.1, -3.1$ mm/year in east and north, DATC $1.0, -2.6$ mm/year and KNID $1.5, -3.6$ mm/year, respectively. The average is $0.8, -3.1$ mm/year in east and north, or equivalent to an extension of 3.2 mm/year across the Gökova rift, along an azimuth $N165^\circ E$ (i.e. NNW–SSE). We note that the geodetically derived azimuth of extension agrees with geological data onshore Kos (NNW–SSE; Kokkalas and Doutsos 2001, their Fig. 9). Moreover, the difference between orientation of regional extension and long-term geological deformation (strike of large faults) can be accommodated by a component of left-lateral slip. Indeed, as the

(fault-controlled) northern coast of the Gökova gulf has an average azimuth of $N85^\circ E$, this implies a minimum component of left-lateral strike-slip of 10° (orthogonal orientation to the NNW–SSE extension is expected at $N75^\circ E$), thus close to the rake value of 15° we find for the slip vector of the 2017 earthquake ($-75^\circ \pm 3$; Table 5).

6.4. Tectonic Implications for the Gökova Rift

According to our joint-inversion model, the seismic fault activated by the 2017 earthquake dips towards the north at a low-to-moderate angle of $37^\circ \pm 3^\circ$ and it accommodates a significant portion

of accumulated strain on the western side of the Gökova rift (i.e. creating accommodation space for young sediments; see findings by Tur et al. 2015 on faster subsidence towards western Gökova). Both fault size and geometry indicate that this is a relatively young structure developed during the Quaternary and represents the main source of seismic hazard in this region. This interpretation is in agreement with the findings of Karasözen et al. (2018). However, we do not share the interpretation put forward by Karasözen et al. (2018) about the existence of a low-angle fault bounding the north shore of Datca peninsula (their Fig. 6, section X–X'). In our tectonic model (Fig. 19) we favour a high-angle fault which we name as *Datca Horst North Boundary 2 Fault* following the terminology of the SHARE project (Basili et al. 2013). Our tectonic model also explains the E–W, splay faults observed in shallow seismic data of the Gokova ridge (Fig. 20) as relatively small structures rooting at the low-angle fault.

The surface projection of the north-dipping seismic fault may be associated with the northern rim of Gökova Ridge (Fig. 19), a 10-km long well-defined, E–W oriented sea-bottom feature (Tur et al. 2015) that is cut by a series of parallel, N-dipping normal faults. In addition, the orientation of the Gökova Ridge fault zone is roughly similar to that of the modelled fault while the up-dip projection of the fault (Fig. 20) crosses the offshore ridge, within limits of small uncertainty variation in the dip value of the model and the width of the fault zone in sea-bottom morphology. Although south-dipping normal faults that border the northern coastline of Gökova Gulf are reported to be the main tectonic features of the Gökova rift (İşcan et al. 2013; Tur et al. 2015), both the 2017 seismic fault geometry and aftershock epicentres (Figs. 11, 12) extending to the north towards the Turkish coast indicate that south-dipping faults close to the Bodrum coast may root on the low-angle fault plane identified in this study (Fig. 19). Moreover, in the area east of Bodrum, seismic slip on north-dipping high-angle faults (60° – 70°) was revealed by relocated aftershocks in this study (Figs. 11, clusters 4 and 5, 12). Based on the aftershock spatial distribution we infer that two of the activated normal faults attain lengths between 5

and 7 km (Fig. 11) and widths between 6 and 8 km (see section e1–e2 in Fig. 12). Such synthetic structures are observed at other young rift terminations (e.g. the Corinth rift) where high-angle normal faults accommodate part of seismic strain in tandem to seismic slip along low-angle faults (Ganas et al. 2013b; Godano et al. 2014; Beckers et al. 2015).

In addition, aftershock epicentres (cluster #1 described previously) weakly delineate a roughly WNW–ESE fault plane dipping north at ci. 40° offshore the north-eastern coast of Kos island, towards the western Bodrum peninsula. We infer the existence of a seismic fault towards the west of the 2017 rupture although more data are needed to better define its geometry and size. Due to the lack of offshore seismic survey data between Kos and Bodrum, its surface trace is roughly projected offshore the Kos coast (in Fig. 19). This area was loaded due to Coulomb stress transfer following the mainshock (Figs. 13, 14, section A–B) with cluster #1 of aftershocks forming immediately after the mainshock (Fig. 16).

Our fault model provides new constraints on active fault mapping inside the Gökova Rift. The inferred north-dipping seismic fault is complementary to fault sources proposed for this area by GreDaSS (Caputo and Pavlides, 2013) and SHARE (Basili et al. 2013) databases. Both databases involve the south dipping *Ula-Ören fault zone* as the main source for the Gökova Gulf (Fig. 19). Based on our geodetic inversion data it is reasonable to constrain the latter SHARE/GreDaSS seismic source for the region west of the longitude 27.60° E (i.e. up to roughly the eastern end of the 2017 seismic fault) as a high-angle structure, antithetic to the low-angle seismic fault. Therefore, the active north-dipping structure revealed by the 2017 earthquake should be incorporated in seismic fault databases of hazardous active structures of the SE Aegean Sea (e.g. Papazachos et al. 2001; Ganas et al. 2013a; Caputo and Pavlides 2013; Sakellariou et al. 2013; Emre et al. 2016).

In addition, more data is needed regarding the south-dipping *Gökova -Oren Fault zone 3* (Fig. 19), which runs parallel to the northern coast for nearly 20 km, to investigate if it comprises of a single active normal fault or it is a synthesis of smaller, high-angle

south-dipping fault segments, antithetic to the main north-dipping fault. We note that its down-dip projection (assuming high-angle geometry) either roots to or dissects the July 20, 2017 fault plane (Fig. 20).

The 2017 fault can fit a structural model, involving the low-angle north-dipping “*Gökova Ridge fault*” as the main structural feature in the western Gökova rift, while high-angle south-dipping faults are antithetic structures that terminate at a depth of about 8–10 km, that is at the junction with or above the north-dipping fault. It is also possible that “blind”, high-angle fault planes that are well defined by triggered aftershocks to the NE of the mainshock’s epicentre (Fig. 11), may intersect the south-dipping normal faults that bound the shoreline of Gökova Gulf such as Gökova-Oren Fault zone 3 (Figs. 19, 20). To investigate if this hypothesis holds, data from local seismic networks need to be collected in the future.

6.5. Seismic Hazard Implications

If we assume that the Kos 2017 earthquake is a characteristic earthquake for this area of the Aegean and on a major fault of the Gökova rift, the ratio of the horizontal co-seismic motion (the heave of the 2017 slip vector; ~ 1.6 m) to the interseismic one (i.e. 3.2 mm/year of opening; calculated at Sect. 6.3) leads to a mean recurrence time of 500 years for large earthquakes ($M > 6$) on that fault. However, if other faults are active and the extension is shared among them (synthetic to the 2017 plane further south or antithetic; see Fig. 19 for probable fault sources), a process known as strain partitioning (e.g. Nicol et al. 2010; Cowie et al. 2012), then the mean recurrence time will be two or three times larger for a single fault in this part of the rift although the mean recurrence interval could be of the order of 500 years for $M_{6.5+}$ earthquakes. It is clear that more data are needed in this area to clarify this.

Furthermore, considering the total length of the Gökova gulf, which is 90 km, if other segments of active faults exist with lengths 15–20 km, thus able to produce events of magnitude similar to the 2017 one, there is space for 5–6 of such segments (aligned E–W along the rift), and therefore “space” for one event of

magnitude 6.5 or more per century (on average) in the Gökova gulf. Those figures are preliminary and could be further evaluated with the help of historical earthquake catalogues, palaeoseismic data and other techniques.

6.6. Relation to Tsunami

The ground deformation towards the east of Bodrum (ancient Halicarnassus) coast was mapped as subsidence due to the fact that the interferograms in both directions (Supplementary Fig. S2 & S3) indicate movement away from the satellite. This InSAR co-seismic “signal” is consistent with the flooding observed at coastal localities according to a field survey and similar reports (e.g. Yalçiner et al. 2017). Post-earthquake field observations mention a first negative wave motion (receding wave) also visible on the IOC tide gauge (<http://www.ioc-sealevelmonitoring.org/station.php?code=bodr>). This observation also agrees with the fault model proposed in this study where the dip-direction of the normal fault is pointing towards Bodrum (Fig. 6) which is located upon the hanging-wall side of the fault. From the same field survey, the largest tsunami damage on the Turkish coast was observed at Gumbet Bay, 3 km west of Bodrum where many boats were damaged and washed onshore. On the Greek coastline flooding was observed in the island of Kos which sustained the largest damage from both the earthquake and tsunami. Streets were flooded and also some boats were washed onshore (Yalçiner et al. 2017; EMSC report). Few eyewitness reports of inundation extent mention as much as 100 m inland but those have not been confirmed. Early estimates indicate smaller inundation extent from the tsunami on the Greek coastlines than what was recorded on the Turkish coast (< 60 m).

The studies of Tiryakioğlu et al. (2018) and Saltogianni et al. (2017) based on teleseismic waveform inversion and geodetic data inversion, propose a southerly dipping fault. However, both geodetic and tsunami observations presented here, contradict that interpretation. More specifically, the suggestion that the hanging-wall is located on the northern side of the gulf (incl. Karaada islet) explains (a) the subsidence observed on geodetic data, (b) the severe flooding

occurred from a moderate-tsunamigenic event on the Turkish coast and not on the side of Kos island and (c) agrees with receding wave motion observed on Gumbet Bay following the earthquake. Furthermore, all reported mainshock epicentre solutions and the relocated solution (Figs. 1, 6) are gathered close to Karaada islet. Such a location is clearly geometrically incompatible with a south-dip geometry. In fact, the epicentre falls out of the surface projection of the south-dip model even if one places it 2 km further south from its relocated determination.

Both recent and strong events near Lesvos ($M_w = 6.3$ June 12, 2017; Ganas et al. 2017b; Briole et al. 2018; Papadimitriou et al. 2018; Kiratzi and Koskosidi 2018) and this one near Kos show that tsunamis can be triggered in the Aegean basin from events that fall below 7.0 or 7.5 in magnitude, which is until now a common cut-off in magnitude for tsunami sources of tectonic origin in many hazard and risk studies (e.g. Geist and Parsons 2005; Geist and Lynett 2014). On the other hand, tsunami observations do not accompany all offshore events of magnitude comparable to Kos 2017 but similar events for which tsunami observational datasets exist (eyewitness accounts or tide gauge records) may help to constrain faults responsible for past events for which parameters are not well resolved. The 2017 field observations confirm that the threat from tsunamis in the Aegean is real and permanent. Serious damage and flooding can follow even relatively small (for tsunamigenesis) tectonic events (e.g. Papadopoulos et al. 2014).

7. Conclusions

(a) We modelled the 2017 seismic fault by combining (1) the GNSS co-seismic offsets, (2) ascending and (3) descending Sentinel 1 interferograms. GNSS constrains very well all fault parameters but does not allow discriminating between the two candidate planes. InSAR strongly supports the north-dipping fault plane solution, and the mixing of ascending and descending interferograms provides an even more robust solution. We find that we can model the overall data with 2.03 m of uniform slip on a

north-dipping normal fault with a small component of left-lateral strike slip.

- (b) The inversion of geodetic data suggests that the upper edge of the fault is offshore, near the Gökova ridge bathymetric feature (Fig. 19), and at relatively shallow depth (2.5 ± 0.2 km), as constrained by the modelling of the GNSS data. Our best fitting fault plane strikes $N283^\circ E$ and dips to the north with an angle of $37^\circ \pm 3^\circ$.
- (c) This fault model is compatible with published seismological data (MT solutions; Table 1) and the spatial distribution of aftershocks following a rigorous relocation procedure (Fig. 12).
- (d) The 2017 fault can fit a structural model, that involves the low-angle north-dipping fault as the main structural feature in the western Gökova rift, while high-angle south-dipping faults are antithetic structures that terminate at a depth of about 8-10 km, on or above the north-dipping fault (Fig. 20).
- (e) Based on analysis of regional GPS data (inter-seismic velocities) we estimated extension across the Gökova gulf after correction of the regional rotation (Fig. 18). We calculated an extension rate of 3.2 mm/year along a direction $N165^\circ E$.
- (f) Assuming a “characteristic-type” of earthquake behaviour for the 2017 seismic fault we obtained a mean recurrence time of 500 years.

Acknowledgements

We are indebted to two anonymous reviewers for their constructive reviews. We thank the NOA, EMSC, KOERI & DDA analysis groups for the provision of seismic data. Sentinel 1A images were provided free by ESA’s Sentinels Scientific Data Hub. Focal mechanism data were accessed from <http://bbnet.gein.noa.gr/HL/>, <http://www.globalcmt.org/>, <http://www.geophysics.geol.uoa.gr/> Bathymetry data were retrieved from EMODNET and topography from ALOS global model (30-m). We thank Ahmed Yalçiner, Evi Nomikou, I. Parcharidis, M. Sachpazi, R. Reilinger, S. Ergintav, T. Taymaz, G. Papadopoulos and E. Lekkas for comments and discussions. We thank the HEPOS network (Greece) for providing

GNSS data from their stations in Kos and Rhodes. We also thank the Greek private networks, METRICANET (<http://www.metricanet.gr/>) and URANUS (TREE Co, <http://www.uranus.gr/>) and the Turkish GCM network for releasing their GNSS data. Coulomb Stress Transfer was calculated by the Coulomb v3.3 software (Toda et al. 2011). Several figures were prepared by use of GMT software (Wessel et al. 2013). P. Argyrakakis acknowledges the Stavros Niarchos Foundation for its support. We acknowledge funding of this research by the project “HELPOS—Hellenic System for Lithosphere Monitoring” (MIS 5002697).

Publisher’s Note Springer Nature remains neutral with regard to jurisdictional claims in published maps and institutional affiliations.

REFERENCES

- Akyol, N., Zhu, L., Mitchell, B. J., Sözbilir, H., & Kekovalı, K. (2006). Crustal structure and local seismicity in western Anatolia. *Geophysical Journal International*, 166(3), 1259–1269. <https://doi.org/10.1111/j.1365-246X.2006.03053.x>.
- Ambraseys, N. N. (2001). Reassessment of earthquakes, 1900–1999, in the Eastern Mediterranean and the Middle East. *Geophysical Journal International*, 145, 471–485. <https://doi.org/10.1046/j.0956-540x.2001.01396.x>.
- Basili, R., Kastelic V., Demircioglu M. B., Garcia Moreno D., Nemser E. S., Petricca P., Sboras S. P., Besana-Ostman G. M., Cabral J., Camelbeeck T., Caputo R., Danciu L., Domac H., Fonseca J., García-Mayordomo J., Giardini D., Glavatic B., Gulen L., Ince Y., Pavlides S., Sesetyan K., Tarabusi G., Tiberti M. M., Utkucu M., Valensise G., Vanneste K., Vilanova S., Wössner J. (2013). The European Database of Seismogenic Faults (EDSF) compiled in the framework of the Project SHARE. <http://diss.rm.ingv.it/share-edsf/>, <https://doi.org/10.6092/ingv.it-share-edsf>.
- Beckers, A., Hubert-Ferrari, A., Beck, C., Bodeux, S., Tripsanas, E., Sakellariou, D., et al. (2015). Active faulting at the western tip of the Gulf of Corinth, Greece, from high-resolution seismic data. *Marine Geology*, 360, 55–69. <https://doi.org/10.1016/j.margeo.2014.12.003>.
- Bertiger, W., et al. (2010). Single receiver phase ambiguity resolution with GPS data. *Journal of Geodesy*, 84(5), 327–337.
- Blewitt, G., Hammond, W. C., & Kreemer, C. (2018). Harnessing the GPS data explosion for interdisciplinary science. *Eos*. <https://doi.org/10.1029/2018EO104623>.
- Briole, P. (2017). Modelling of earthquake slip by inversion of GNSS and InSAR data assuming homogenous elastic medium. *Zenodo*. <https://doi.org/10.5281/zenodo.1098399>.
- Briole, P. et al. (2018). The June 12, 2017 M6.3 Lesvos offshore earthquake sequence (Aegean Sea, Greece): Fault model and ground deformation from seismic and geodetic observations. EGU General Assembly Conference Abstracts 20, 18189.
- Briole, P., De Natale, G., Gaulon, R., Pingue, F., & Scarpa, R. (1986). Inversion of geodetic data and seismicity associated with the Friuli earthquake sequence (1976–1977). *Annales Geophysicae*, 4(B4), 481–492.
- Briole, et al. (2015). The seismic sequence of January–February 2014 at Cephalonia Island (Greece): Constraints from SAR interferometry and GPS. *Geophysical Journal International*, 203(3), 1528–1540. <https://doi.org/10.1093/gji/ggv353>.
- Brüstle, A., (2012). Seismicity of the eastern Hellenic Subduction Zone, PhD thesis, Ruhr-Universität, Bochum.
- Caputo, R., Pavlides, S. (2013). The Greek Database of Seismogenic Sources (GreDaSS), version 2.0.0: A compilation of potential seismogenic sources (Mw > 5.5) in the Aegean Region. <http://gredass.unife.it/>, <https://doi.org/10.15160/unife/gredass/0200>
- Cattin, R., Briole, P., Lyon-Caen, H., Bernard, P., & Pinettes, P. (1999). Effects of superficial layers on coseismic displacements for a dip-slip fault and geophysical implications. *Geophysical Journal International*, 137, 149–158. <https://doi.org/10.1046/j.1365-246x.1999.00779.x>.
- Cowie, P. A., Roberts, G. P., Bull, J. M., & Visini, F. (2012). Relationships between fault geometry, slip rate variability and earthquake recurrence in extensional settings. *Geophysical Journal International*, 189, 143–160. <https://doi.org/10.1111/j.1365-246X.2012.05378.x>.
- Das, S., & Henry, C. (2003). Spatial relation between main earthquake slip and its aftershock distribution. *Reviews of Geophysics*, 41(3), 1013. <https://doi.org/10.1029/2002RG000119>.
- EGELADOS project at Ruhr-University Bochum web site <http://www.gmg.ruhr-uni-bochum.de/geophysik/seismology/research/egelados.html> (last accessed Nov. 28, 2018)
- Elliott, J. R., Nissen, E. K., England, P. C., Jackson, J. A., Lamb, S., Li, Z., et al. (2012). Slip in the 2010–2011 Canterbury earthquakes, New Zealand. *Journal of Geophysical Research*, 117, B03401. <https://doi.org/10.1029/2011JB008868>.
- Emre, Ö., Duman, T. Y., Özalp, S., et al. (2016). Active fault database of Turkey. *Bull Earthquake Eng*, 2, 44. <https://doi.org/10.1007/s10518-016-0041-2>.
- Feng, W., Tian, Y., Zhang, Y., Samsonov, S., Almeida, R., & Liu, P. (2017). A Slip Gap of the 2016 Mw 6.6 Muji, Xinjiang, China, Earthquake Inferred from Sentinel-1 TOPS Interferometry. *Seismological Research Letters*, 88, 1054–1064. <https://doi.org/10.1785/0220170019>.
- Floyd, M. A., et al. (2010). A new velocity field for Greece: Implications for the kinematics and dynamics of the Aegean. *Journal of Geophysical Research*, 115, B10403. <https://doi.org/10.1029/2009JB007040>.
- Friederich, W., Brüstle, A., Küperkoch, L., & Meier, T. (2013). Focal mechanisms in the Southern Aegean from temporary seismic networks—Implications for the regional stress field and ongoing deformation processes. *Solid Earth Discuss*, 5, 1721–1770. <https://doi.org/10.5194/sed-5-1721-2013>.
- Ganas et al. (2017a). Co-seismic deformation and preliminary fault model of the July 20, 2017 M6.6 Kos earthquake, Aegean Sea. Report published on 30 July 2017 with EMSC https://www.emsc-csem.org/Files/event/606346/Kos_report_30-7-2017.pdf

- Ganas, A. et al. (2018). The July 20, 2017 M6.6 Kos-Bodrum earthquake: seismic and geodetic evidence for a north-dipping, normal fault at the western end of the Gulf of Gökova, SE Aegean Sea. *Geophysical Research Abstracts* 20, EGU2018-9262.
- Ganas, A., Briole, P., Elias, P., Korkouli, P., Moshou, A., Valkaniotis, S., Rogier, M., Foulmelis, M., Argyrakakis, P., Parcharidis, I. (2017b). Preliminary characteristics of the June 12, 2017 M6.3 Plomari earthquake sequence (Lesvos, Greece) from seismic and geodetic data, Safe Athens 2017 Book of Abstracts, page 16.
- Ganas, A., Chousianitis, K., Batsi, E., Kolligri, M., Agalos, A., Chouliaras, G., et al. (2013a). The January 2010 Efpalion earthquakes (Gulf of Corinth, Central Greece): earthquake interactions and blind normal faulting. *Journal of Seismology*, 17(2), 465–484. <https://doi.org/10.1007/s10950-012-9331-6>.
- Ganas, A., Chousianitis, K., Drakatos, G., Papanikolaou, M., Argyrakakis, P. & Kolligri, M. (2011). NOANET: High-rate GPS Network for Seismology and Geodynamics in Greece. *Geophysical Research Abstracts*, Vol. 13, EGU2011-4840, 2011, EGU General Assembly 2011.
- Ganas, A., Drakatos, G., Rontogianni, S., Tsimi, C., Petrou, P., & Papanikolaou, M. (2008). NOANET: The new permanent GPS network for Geodynamics in Greece. *Geophysical Research Abstracts*, Vol. 10, EGU2008-A-04380.
- Ganas, A., Oikonomou, A., & Tsimi, C. (2013b). NOAfaults: A digital database for active faults in Greece. *Bulletin Geological Soc*, 47, 518–530. <https://doi.org/10.12681/bgsg.11079>.
- Ganas, A., & Parsons, T. (2009). Three-dimensional model of Hellenic Arc deformation and origin of the Cretan uplift. *Journal of Geophysical Research*, 114, B06404. <https://doi.org/10.1029/2008JB005599>.
- Ganas, A., Sokos, E., Agalos, A., Leontakianakos, G., & Pavlides, S. (2006). Coulomb stress triggering of earthquakes along the Atalanti Fault, central Greece: Two April 1894 M6 + events and stress change patterns. *Tectonophysics*, 420, 357–369.
- Geist, E., & Lynett, P. (2014). Source process in the probabilistic assessment of Tsunami hazards. *Oceanography*, 27(2), 86–93. <https://doi.org/10.5670/oceanog.2014.43>.
- Geist, E. L., & Parsons, T. (2005). Probabilistic analysis of tsunami hazards. *Natural Hazards*, 37(3), 277–314.
- Gianniou, M. (2011). *Detecting permanent displacements caused by earthquakes using data from the HEPOS network, EUREF 2011 Symposium, May 25-28 2011*. Moldova: Chisinau.
- Godano, M., Deschamps, A., Lambotte, S., Lyon-Caen, H., Bernard, P., & Pacchiani, F. (2014). Focal mechanisms of earthquake multiplets in the western part of the Corinth Rift (Greece): influence of the velocity model and constraints on the geometry of the active faults. *Geophysical Journal International*, 197, 1660–1680. <https://doi.org/10.1093/gji/ggu059>.
- Görür, N., Şengör, A. M. C., Sakıncı, M., Tüysüz, O., Akkök, R., Yiğitbaş, E., et al. (1995). Rift formation in the Gökova region, southwest Anatolia: Implications for the opening of the Aegean Sea. *Geological Magazine*, 132, 637–650.
- USGS <https://earthquake.usgs.gov/earthquakes/eventpage/us20009ynd#moment-tensor>
- Grigoriadis, V. N., Tziavos, I. N., Tsokas, G. N., & Stampolidis, A. (2016). Gravity data inversion for Moho depth modeling in the Hellenic area. *Pure and Applied Geophysics*, 173, 1223–1241. <https://doi.org/10.1007/s00024-015-1174-y>.
- Gürer, Ö. F., Sangu, E., Özburan, M., Gürbüz, A., & Sarıca-Filoreau, N. (2013). Complex basin evolution in the Gökova Gulf region: implications on the Late Cenozoic tectonics of SW Turkey. *International Journal of Earth Sciences*, 25, 24. <https://doi.org/10.1007/s00531-013-0909-1>.
- Gürer, Ö. F., & Yılmaz, Y. (2002). Geology of the Ören and surrounding areas, SW Anatolia. *Turkish Journal of Earth Sciences*, 11, 1–13.
- Howell, A., Jackson, J., Copley, A., McKenzie, D., & Nissen, E. (2017). Subduction and vertical coastal motions in the eastern Mediterranean. *Geophysical Journal International*, 211(1), 593–620. <https://doi.org/10.1093/gji/ggx307>.
- Irmak, S. (2013). Focal mechanisms of small-moderate earthquakes in Denizli Graben (SW Turkey). *Earth Planets Space*, 65, 943–955.
- İşcan, Y., Tur, H., & Göktaşan, E. (2013). Morphologic and seismic features of the Gulf of Gökova, SW Anatolia: Evidence of strike-slip faulting with compression in the Aegean extensional regime. *Geo-Marine Letters*, 33(1), 31–48.
- Kapetanidis, V. (2017). Spatiotemporal patterns of microseismicity for the identification of active fault structures using seismic waveform cross-correlation and double-difference relocation. PhD dissertation, National and Kapodistrian University of Athens.
- Karakonstantis, A. (2017). 3-D simulation of crust and upper mantle structure in the broader Hellenic area through Seismic Tomography. PhD dissertation, National and Kapodistrian University of Athens (in Greek).
- Karasözen, E., et al. (2018). The 2017 July 20 Mw 6.6 Bodrum-Kos earthquake illuminates active faulting in the Gulf of Gökova, SW Turkey. *Geophysical Journal International*, 214(1), 185–199. <https://doi.org/10.1093/gji/ggy114>.
- King, G. C. P., Stein, R. S., & Lin, J. (1994). Static stress changes and the triggering of earthquakes. *Bulletin of the Seismological Society of America*, 84(3), 935–953.
- Kiratzis, A., & Koskosidi, A. (2018). Constraints on the near-source motions of the Kos-Bodrum 20 July 2017 Mw6.6 earthquake, 16th ECEE conference, Thessaloniki.
- Kiratzis, A., & Louvari, E. (2003). Focal mechanisms of shallow earthquakes in the Aegean Sea and the surrounding lands determined by waveform modelling: a new database. *Journal of Geodynamics*, 36(1–2), 251–274.
- Kissling, E., Ellsworth, W. L., Eberhart-Phillips, D., & Kradolfer, U. (1994). Initial reference models in local earthquake tomography. *Journal of Geophysical Research*, 99, 19635–19646. <https://doi.org/10.1029/93JB03138>.
- Klein, F. W. (1989). User's guide to HYPOINVERSE, a program for VAX computers to solve earthquake locations and magnitudes. *U.S Geological Survey Open-File Report*, 89–314, 1–58.
- Kokkalas, S., & Doutsos, T. (2001). Strain-dependent stress field and plate motions in the south-east Aegean region. *Journal of Geodynamics*, 32(3), 311–332. [https://doi.org/10.1016/S0264-3707\(01\)00035-7](https://doi.org/10.1016/S0264-3707(01)00035-7).
- Konca, A. O. et al. (2018). The Geometry and Coseismic Slip of 2017 Mw 6.6 Bodrum-Kos Earthquake Inferred from Geodetic, Seismic Data and Aftershocks, *Geophysical Research Abstracts*, Vol. 20, EGU2018-7442.
- Kouskouna, V., Sesetyan, K., & Stucchi, M. (2017). The 1933 Kos earthquake: a preliminary study, Gruppo Nazionale di Geofisica della Terra Solida 36o Convegno Nazionale, 14-16/11/2017, Trieste.
- Kreemer, C., & Chamot-Rooke, N. (2004). Contemporary kinematics of the southern Aegean and the Mediterranean Ridge.

- Geophysical Journal International*, 157, 1377–1392. <https://doi.org/10.1111/j.1365-246X.2004.02270.x>.
- Kurt, H., Demirbağ, E., & Kuşçu, İ. (1999). Investigation of the submarine active tectonism in the Gulf of Gökova, southwest Anatolia–southeast Aegean Sea, by multi-channel seismic reflection data. *Tectonophysics*, 305, 477–496.
- Makropoulos, K., Kaviris, G., & Kouskouna, V. (2012). An updated and extended earthquake catalogue for Greece and adjacent areas since 1900. *Natural Hazards and Earth Systems Sciences*, 12, 1425–1430.
- Melgar, D., Ganas, A., Geng, J., Liang, C., Fielding, E. J., & Kassaras, I. (2017). Source characteristics of the 2015 Mw 6.5 Lefkada, Greece, strike-slip earthquake. *Journal of Geophysical Research: Solid Earth*. <https://doi.org/10.1002/2016JB013452>.
- Nicol, A., Walsh, J., Villamor, P., Seebeck, H., & Berryman, K. R. (2010). Normal fault interactions, paleoearthquakes and growth in an active rift. *Journal of Structural Geology*, 32, 1101–1113.
- Nomikou, P. (2004). Geodynamic of Dodecanese Islands: Kos and Nisyros Volcanic Field. PhD thesis Department of Geology and Geoenvironment, University of Athens, p. 470.
- Nomikou, P., & Papanikolaou, D. (2011). Extension of active fault zones on Nisyros volcano across the Yali-Nisyros Channel based on onshore and offshore data. *Marine Geophysical Researches*, 32(1/2), 181–192. <https://doi.org/10.1007/s11001-011-9119-z>.
- Nomikou, P., Papanikolaou, D., Alexandri, M., Sakellariou, D., & Rousakis, G. (2013). Submarine volcanoes along the Aegean volcanic arc. *Tectonophysics*, 597–598, 123–146. <https://doi.org/10.1016/j.tecto.2012.10.001>.
- Ocakoglu, N., Nomikou, P., İşcan, Y., et al. (2018). Evidence of extensional and strike-slip deformation in the offshore Gökova-Kos area affected by the July 2017 Mw 6.6 Bodrum-Kos earthquake, eastern Aegean Sea. *Geo-Marine Letters*, 38, 211. <https://doi.org/10.1007/s00367-017-0532-4>.
- Okada, Y. (1992). Internal deformation due to shear and tensile faults in a half space. *Bulletin of the Seismological Society of America*, 82, 1018–1040.
- Panagiotopoulos, D. G. (1984). Travel time curves and crustal structure in the southern Balkan region, PhD thesis, Aristotle Univ. of Thessaloniki, Thessaloniki, p. 159 (in Greek).
- Papadimitriou, P., Chousianitis, K., Agalos, A., Moshou, A., Lagios, E., & Makropoulos, K. (2012). The spatially extended 2006 April Zakynthos (Ionian Islands, Greece) seismic sequence and evidence for stress transfer. *Geophysical Journal International*, 190, 1025–1040. <https://doi.org/10.1111/j.1365-246X.2012.05444.x>.
- Papadimitriou, P., Kassaras, I., Kaviris, G., Tselentis, G.-A., Voulgaris, N., Lekkas, E., et al. (2018). The 12th June 2017 Mw=6.3 Lesbos earthquake from detailed seismological observations. *Journal of Geodynamics*, 115, 23–42. <https://doi.org/10.1016/j.jog.2018.01.009>.
- Papadopoulos, G., et al. (2014). Historical and pre-historical tsunamis in the Mediterranean and its connected seas: Geological signatures, generation mechanisms and coastal impacts. *Marine Geology*, 354, 81–109.
- Papanikolaou, D. J., & L. H. Royden (2007). Disruption of the Hellenic arc: Late Miocene extensional detachment faults and steep Pliocene-Quaternary normal faults—Or what happened at Corinth? *Tectonics*, 26, TC5003, <https://doi.org/10.1029/2006tc002007>.
- Papathassiou, G., Valkaniotis, S., & Pavlides, S. (2019). The July 20, 2017 Bodrum-Kos, Aegean Sea Mw = 6.6 earthquake: preliminary field observations and image-based survey on a lateral spreading site. *Soil Dynamics and Earthquake Engineering*, 116, 668–680. <https://doi.org/10.1016/j.soildyn.2018.10.038>.
- Papazachos, B. C., Mountrakis, D. M., Papazachos, C. B., Tranos, M. D., Karakaisis, G. F., and Savvaidis, A. S. (2001). The faults which have caused the known major earthquakes in Greece and surrounding region between the 5th century BC and today. In Proceedings of 2nd National Conference Anti-Seismic Engineering and Technical Seismology, 17–26, Technical Chamber of Greece, Thessaloniki, Greece.
- Papazachos, B. C., & Papazachou, C. B. (1997). *The earthquakes of Greece* (p. 304). Thessaloniki: Ziti Publ.
- Parsons, T. (2005). A hypothesis for delayed dynamic earthquake triggering. *Geophysical Research Letters*. <https://doi.org/10.1029/2004gl021811>.
- Reilinger, R., McClusky, S., Paradissis, D., Ergintav, S., & Vernant, P. (2010). Geodetic constraints on the tectonic evolution of the Aegean region and strain accumulation along the Hellenic subduction zone. *Tectonophysics*, 488(1–4), 22–30. <https://doi.org/10.1016/j.tecto.2009.05.027>.
- Reilinger, R., McClusky, S., Vernant, P., et al. (2006). GPS constraints on continental deformation in the Africa–Arabia–Eurasia continental collision zone and implications for the dynamics of plate interactions. *Journal of Geophysical Research: Solid Earth*. <https://doi.org/10.1029/2005jb004051>.
- Sakellariou, D., Mascle, J., & Lykousis, V. (2013). Strike slip tectonics and transtensional deformation in the Aegean region and the Hellenic arc: Preliminary results. *Bulletin of the Geological Society of Greece*, 47, 647–656.
- Saltogianni, V., Taymaz, T., Yolsal-Cevikbilen, S., Eken, T., Gianniu, M., Ocalan, T., et al. (2017). *Fault-model of the 2017 Kos-Bodrum (east Aegean Sea) Mw 6.6 earthquake from inversion of seismological and GPS data—Preliminary Report*. EMSC. <http://www.emsc-csem.org>.
- Sodoudi, F., Kind, R., Hatzfeld, D., Priestley, K., Hanka, W., Wylegalla, K., et al. (2006). Lithospheric structure of the Aegean obtained from P and S receiver functions. *Journal of Geophysical Research: Solid Earth*, 111, B12307. <https://doi.org/10.1029/2005JB003932>.
- Sokos, E., & Zahradnik, Jiri. (2008). ISOLA a Fortran code and a Matlab GUI to perform multiple-point source inversion of seismic data. *Computers & Geosciences*, 34(8), 967–977. <https://doi.org/10.1016/j.cageo.2007.07.005>.
- Tibaldi, A., Pasquarè, F. A., Papanikolaou, D., & Nomikou, P. (2008). Tectonics of Nisyros Island, Greece, by field and offshore data, and analogue modeling. *Journal of Structural Geology*, 30(12), 1489–1506.
- Tirel, C., Gueydan, F., Tiberi, C., & Brun, J.-P. (2004). Aegean crustal thickness inferred from gravity inversion. Geodynamical implications. *Earth and Planetary Science Letters*, 228, 267–280. <https://doi.org/10.1016/j.epsl.2004.10.023>.
- Tiryakioğlu, İ., Aktuğ, B., Yiğit, C. Ö., Yavaşoğlu, H. H., Sözbilir, H., Özkaymak, Ç., et al. (2018). Slip distribution and source parameters of the 20 July 2017 Bodrum-Kos earthquake (Mw 6.6) from GPS observations. *Geodinamica Acta*, 30(1), 1–14. <https://doi.org/10.1080/09853111.2017.1408264>.
- Toda, S., Stein, R. S., Sevilgen, V., Lin, J. (2011). Coulomb 3.3 Graphic-rich deformation and stress-change software for earthquake, tectonic, and volcano research and teaching-user guide. U.S. Geological Survey Open-File Report 2011-1060, 63, <http://pubs.usgs.gov/of/2011/1060/>

- Tur, H., et al. (2015). Pliocene-Quaternary tectonic evolution of the Gulf of Gökova, southwest Turkey. *Tectonophysics*. <https://doi.org/10.1016/j.tecto.2014.11.008>.
- Ulug, A., Duman, M., Ersoy, S., Özel, E., & Mert Avci, M. (2005). Late Quaternary sea level change, sedimentation and neotectonics of the Gulf of Gökova: Southeastern Aegean Sea. *Marine Geology*, 221(1–4), 381–395. <https://doi.org/10.1016/j.margeo.2005.03.002>.
- Vernant, P., Reilinger, R., & McClusky, S. (2014). Geodetic evidence for low coupling on the Hellenic subduction plate interface. *Earth and Planetary Science Letters*, 385(385), 122–129. <https://doi.org/10.1016/j.epsl.2013.10.018>.
- Wadati, K. (1933). On the travel time of earthquake waves. Part. II. *Geophysical Magazine*, 7, 101–111.
- Waldhauser, F. (2001). HypoDD—A program to compute double-difference hypocentre locations. U.S. Geol. Surv. Open File Rep. 01–113, 25 p.
- Wang, R., Xia, Y., Grosser, H., Wetzel, H.-U., Kaufmann, H., & Zschau, J. (2004). The 2003 Bam (SE Iran) earthquake: precise source parameters from satellite radar interferometry. *Geophysical Journal International*, 159(3), 917–922. <https://doi.org/10.1111/j.1365-246X.2004.02476.x>.
- Ward, J. H. (1963). Hierarchical grouping to optimize an objective function. *Journal of American Statistical Association*, 58, 236–244. <https://doi.org/10.1080/01621459.1963.10500845>.
- Wells, D. L., & Coppersmith, K. J. (1994). New empirical relationships among magnitude, rupture width, rupture area, and surface displacement. *Bulletin of the seismological Society of America*, 84, 974–1002.
- Wessel, P., Smith, W. H. F., Scharroo, R., Luis, J. F., & Wobbe, F. (2013). Generic mapping tools: Improved version released, EOS Trans. *AGU*, 94, 409–410.
- Yalçın, A., Annunziato, A., Papadopoulos, G., Güney-Doğan, G., Gökhan-Güler, H., Erayçakır, T., Özer-Sözünler, C., Ulutaş, E., Arikawa, T., Süzen, L., Kanoğlu, U., Güler, I., Probst, P., Synolakis, C. (2017). The 20th July 2017 (22:31 UTC) Bodrum-Kos Earthquake and Tsunami: Post Tsunami Field Survey Report, <http://users.metu.edu.tr/yalciner/July-21-2017-tsunami-report/Report-Field-Survey-of-July-20-2017-Bodrum-Kos-Tsunami.pdf>
- Yolsal-Çevikbilen, S., Taymaz, T., Helvacı, C. (2014). Earthquake mechanisms in the Gulfs of Gökova, Sığacık, Kuşadası, and the Simav Region (western Turkey): Neotectonics, seismotectonics and geodynamic implications. *Tectonophysics*, 635, 100–124. <https://doi.org/10.1016/j.tecto.2014.05.001>.
- Zhu, L., Mitchell, B. J., Akyol, N., Cemen, I., & Kekovali, K. (2006). Crustal thickness variations in the Aegean region and implications for the extension of continental crust. *Journal of Geophysical Research*, 111, B01301. <https://doi.org/10.1029/2005JB003770>.
- Zumberge, J. F., Heflin, M. B., Jefferson, D. C., Watkins, M. M., & Webb, F. H. (1997). Precise point positioning for the efficient and robust analysis of GPS data from large networks. *Journal of Geophysical Research*, 102(B3), 5005–5018.

(Received August 3, 2018, revised March 2, 2019, accepted March 7, 2019)